INL/EXT-16-38324
Revision 0

Evaluation of Erosion of the Dummy "EE" Plate 19 in YA Type ATR Fuel Element During Reactor PALM Cycles

Jeffrey O. Brower
Michael V. Glazoff
Thomas J. Eiden
Aleksey V. Rezvoi

August 2016

The INL is a
U.S. Department of Energy
National Laboratory
operated by
Battelle Energy Alliance

INL/EXT-16-38324
Revision 0

Evaluation of Erosion of the Dummy "EE" Plate 19 in YA Type ATR Fuel Element During Reactor PALM Cycles

Jeffrey O. Brower
Michael V. Glazoff
Thomas J. Eiden
Aleksey V. Rezvoi

August 2016

Idaho National Laboratory
Advanced Test Reactor
Idaho Falls, Idaho 83415

http://www.inl.gov

Prepared for the
U.S. Department of Energy
Office of Nuclear Energy
Under DOE Idaho Operations Office
Contract DE-AC07-05ID14517

Advanced Test Reactor

Evaluation of Erosion of the Dummy "EE" Plate 19 in YA Type ATR Fuel Element During Reactor PALM Cycles

INL/EXT-16-38324
Revision 0

August 2016

Author:

Jeffrey O. Brower
Project Manager, ATR Fuel Management Support
Date: 8/17/16

Michael V. Glazoff, Ph.D.
Staff Scientist. Energy Systems Integration
Date: 8/17/16

Aleksey V. Rezvoi
Nuclear Engineer, ATR Reactor Engineering
Date: 8/17/16

Thomas J. Eiden
Nuclear Engineer, ATR Reactor Engineering
Date: 8/17/16

Approved by:

Name: RYAN LITTLE
Title: ATR REACTOR & NUCLEAR SAFETY ENGINEERING MANAGER
Date: 8/18/16

ABSTRACT

Advanced Test Reactor (ATR) Cycle 153B-1 was a 14-day, high-power, powered axial locator mechanism (PALM) operating cycle that completed on April 12, 2013. Cycle 153B-1 was a typical operating cycle for the ATR and did not result in any unusual plant transients. ATR was started up and shut down as scheduled. The PALM drive physically moves the selected experiments into and out of the core to simulate reactor startup and heat up, and shutdown and cooldown transients, while the reactor remains in steady state conditions. However, after the cycle was over, when the fuel elements were removed from the core and inspected, several thousand flow-assisted erosion pits and "horseshoeing" defects were readily observed on the surface of the several YA-type fuel elements (these are aluminum "dummy" plates that contain no fuel).

In order to understand these erosion phenomena a thermal-hydraulic model of coolant channel 20 on a YA-M fuel element was generated. The boundaries of the model were the aluminum EE plate of a YA-M fuel element and a beryllium reflector block with 13 horizontal saw cuts which represented regions of zero flow. The heat generated in fuel plates 1 through 18 was modeled to be passing through the aluminum EE plate. The coolant channel 20 width was set at 0.058 in. (58 mils). It was established that the horizontal saw cuts had a significant effect on the temperature of the coolant.

The flow, which was expected to vary linearly with gradual heating of the coolant as it passed through the channel, was extremely turbulent. The temperature rise, which was expected to be a smooth "S" curve, was represented by a series temperature rise "humps," which occurred at each horizontal saw cut in the beryllium reflector block. Each of the 13 saw cuts had a chamfered edge which resulted in the coolant flow being re-directed as a jet across the coolant channel into the surface of the EE plate, which explained the temperature rise and the observed scalloping and pitting degradation on the YA-M fuel elements. In the case of scalloping (horseshoeing) a surprising similarity of that defect to those appearing on aluminum plate rolled in over-lubrication conditions, were established. In turn, this made us think that the principal feature responsible for the appearance of these defects, was horizontal cuts in the beryllium reflector block created to arrest the propagation of large vertical crack(s) in Be in PALM cycles with higher overall fluence. This assumption was fully confirmed by the results of thermo-hydraulic simulations. The neutronics data for these modeling experiments were provided using advanced irradiation simulations (MCNP, HELIOS).

In the case of pitting erosion the following corrective measures were proposed based upon the results of JMatPro v.8.2 modeling (TTT- and CCT-diagrams): change the fabrication process by adding blister anneal before program anneal, immediately after cold rolling of AA6061plate. This step will allow achieving complete recrystallization, eliminating of strengthening due to metastable precipitates, and reduce the possibility of forming sharp microstructural features upon the surface.

ACKNOWLEDGEMENTS

The authors would like to express their sincere gratitude to the many Colleagues at the Idaho National Laboratory who have actively contributed to the successful completion of this project: Mr. Ronald E. Mizia (INL, retired), Mr. Eric Shaber (INL, retired), Mr. Nicolas Woolstenhulme, and Mr. Clinton “Dana” Cooper for their critical comments and the discussion of the problem and the manuscript.

This information was prepared as an account of work sponsored by an agency of the U.S. Government. Neither the U.S. Government nor any agency thereof, nor any of their employees, makes any warranty, expressed or implied, or assumes any legal liability or responsibility for the accuracy, completeness, or usefulness, of any information, apparatus, product, or process disclosed, or represents that its use would not infringe privately owned rights. References herein to any specific commercial product, process, or service by trade name, trade mark, manufacturer, or otherwise, does not necessarily constitute or imply its endorsement, recommendation, or favoring by the U.S. Government or any agency thereof. The views and opinions of authors expressed herein do not necessarily state or reflect those of the U.S. Government or any agency thereof.

CONTENTS

FIGURES

TABLES

ACRONYMS

ATR	Advanced Test Reactor
BWXT	BWX Technologies, Inc.
CCT	Continuous Cooling Diagram
CIC	Core internal changeout
EE	Aluminum “dummy” plate
Ft/s	feet/second
FY	Fiscal Year
HELIOS	Reactor Neutronics Modeling Code
MCNP	Monte-Carlo Simulation Code
MW	Megawatts
NCR	nonconformance report
NE	northeast
NOG	Nuclear Operations Group
NW	northwest
PALM	powered axial locator mechanism
PCPs	primary coolant pumps
SAR	Safety Analysis Report
SE	southeast
SPP	second-phase particles
STAR-CCM+	CFD modeling code
TEV	Technical Evaluation Report
TTT	Time-Temperature-Transformation diagram
UFSAR	Upgraded Final Safety Analysis Report
YA	Aluminum “dummy” element (in the reactor)

Evaluation of Erosion of the Dummy "EE" Plate 19 in YA Type ATR Fuel Element During Reactor PALM Cycles

1. DESCRIPTION OF EROSION EVENT

Advanced Test Reactor (ATR) Cycle 153B-1 was a 14-day, high-power, powered axial locator mechanism (PALM) operating cycle that completed on April 12, 2013. Cycle 153B-1 was a typical operating cycle for the ATR and did not result in any unusual plant transients. ATR was started up and shut down as scheduled. The PALM drive physically moves the selected experiments into and out of the core to simulate reactor startup and heat up, and shutdown and cooldown transients, while the reactor remains in steady state conditions [1-5].

After 14 days of power operation, the reactor was shut down as scheduled to begin a planned refueling and maintenance outage. All 40 of the fuel elements loaded in the core were removed and visually inspected. Eight previously new YA-M type ATR fuel elements [1, 6, 7] were observed to have significant pitting degradation on plate 19. Plate 19 on a YA-M fuel element is an aluminum "dummy" plate, without any fuel material, fabricated to replace the fuel plate 19 in a standard XA/7F type fuel element. The fuel fabricator BWX Technologies, Inc. (BWXT) Nuclear Operations Group (NOG) in Lynchburg, VA identifies this aluminum "dummy" plate as an "EE" plate during fuel fabrication. The ATR Canal Operators described the dummy plates on these YA-M fuel elements as being "scaly" or "pitted" in appearance. Upon closer examination, thousands of flow erosion/corrosion pits were readily visible over approximately 40 inches of the 49.5-inch-long exterior surface of the EE plate on each of the previously new YA-M type fuel elements. The top 4 inches and bottom 4 inches of plate 19 were smooth. Similar pitting degradation was not observed on the exposed surface of plate 1 or the side plates of these YA-M type fuel elements, nor was any pitting degradation observed on any of the standard XA/7F fuel elements that had been loaded in the core, including those that were loaded immediately adjacent to the YA-M fuel elements [1-5]. The interior surface of plate 19 and none of the other fuel plates (plate 2 - 18) can be visually inspected [6-10]

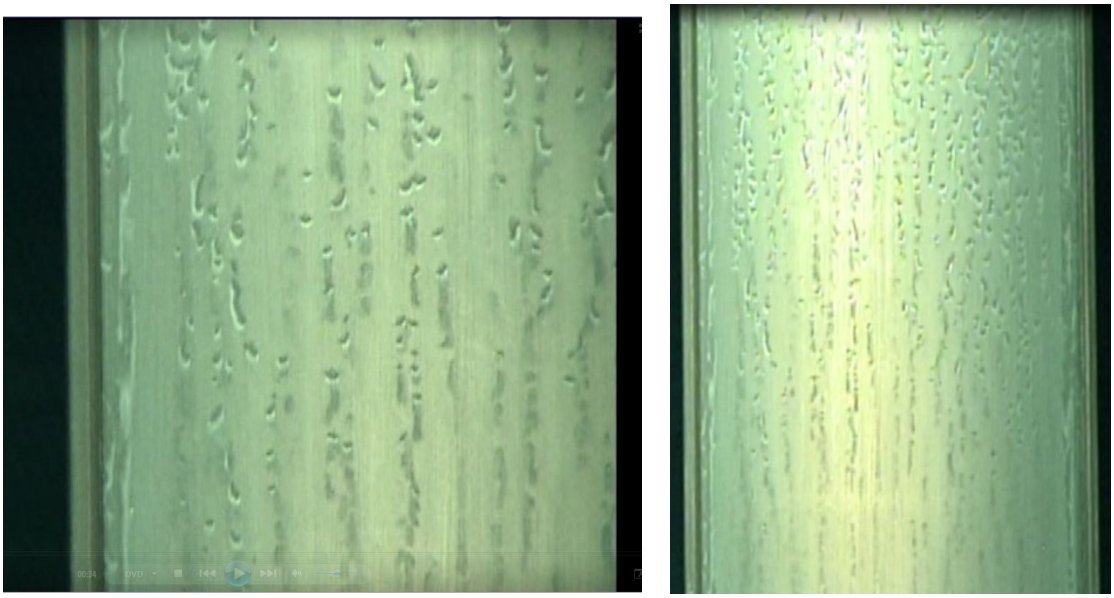

Figure 1. Corroded dummy plate – photographs taken after the fuel elements were removed from the reactor.

Yet another, very different type of erosion was also observed, see Figure 2:

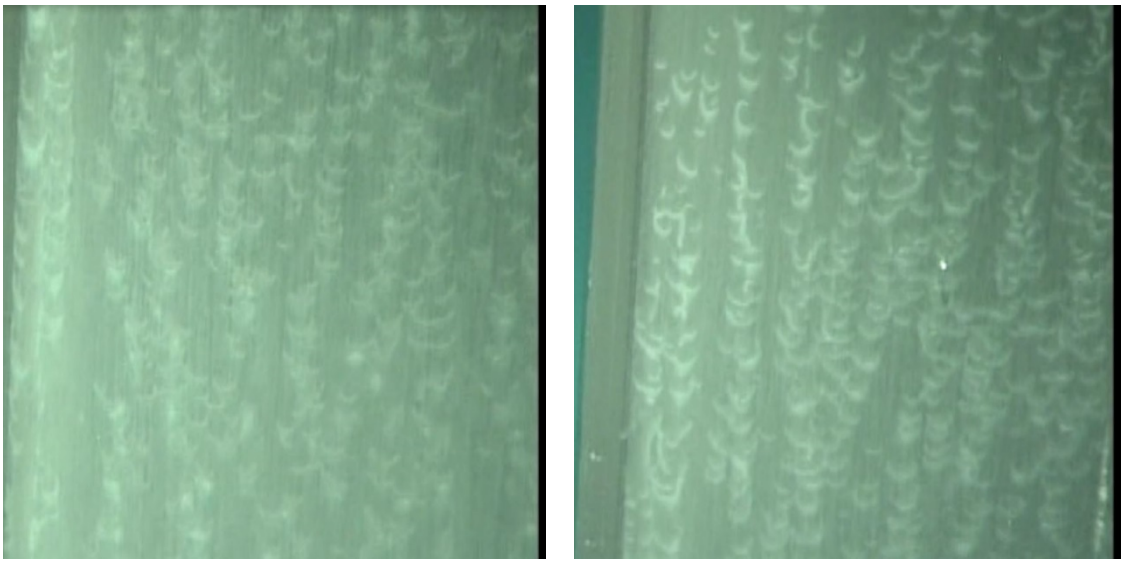

Figure 2. “Scalloping,” or horseshoeing erosion - 6061 “dummy” plate

There were numerous unique conditions that occurred during cycle 153B-1 that may have contributed to the observed pitting degradation:

1. Higher reactor power – 180 MW vs. 110 MW
2. Higher lobe power – 55 MW vs. 23 MW
3. Higher flux tilt across the core – 55 MW SW lobe vs. 20 MW NE and NW lobes
4. Higher flow rates – 3 primary coolant pumps (PCPs) vs. 2 PCPs
5. Higher flow velocities – 47 feet/second (ft/s) vs. 43 ft/s
6. Transient core conditions for experiments – PALM vs. steady state
7. Beryllium age – late in core internal changeout (CIC) life vs. early in CIC life
8. Undetected changes in ATR primary coolant or canal water chemistry
9. Different fuel element type – YA-M vs. XA/7F
10. Coolant channel 20 width – 0.073 in. vs. 0.058 in. due to modified side plates
11. Plate 19 – Aluminum “dummy” plate vs. fuel plate
12. Power density – 18 fuel plates vs. 19 fuel plates
13. Plate fabrication –cold roll vs. hot roll
14. Lower temperature annealing process –Program anneal vs. Blister anneal
15. Possible changes in the fabrication process
16. Contaminants introduced during the fabrication process – 2005 vs. 2014 production runs.

1.1 ATR Fuel Element Design and Fabrication

Each ATR fuel element consists of 19 parallel curved fuel plates attached to two side plates to form a 45-degree sector of a right circular cylinder. Plate 1 is the smallest of the 19 plates, and plate 19 is the largest of the plates. Each fuel element has 20 coolant channels with Channel 1 on the inner radius of Plate 1, Channels 2 through 19 between adjacent fuel plates, and Channel 20 on the outer radius of Plate 19. A schematic of the AA6061-clad nuclear fuel element is presented in Figure 3:

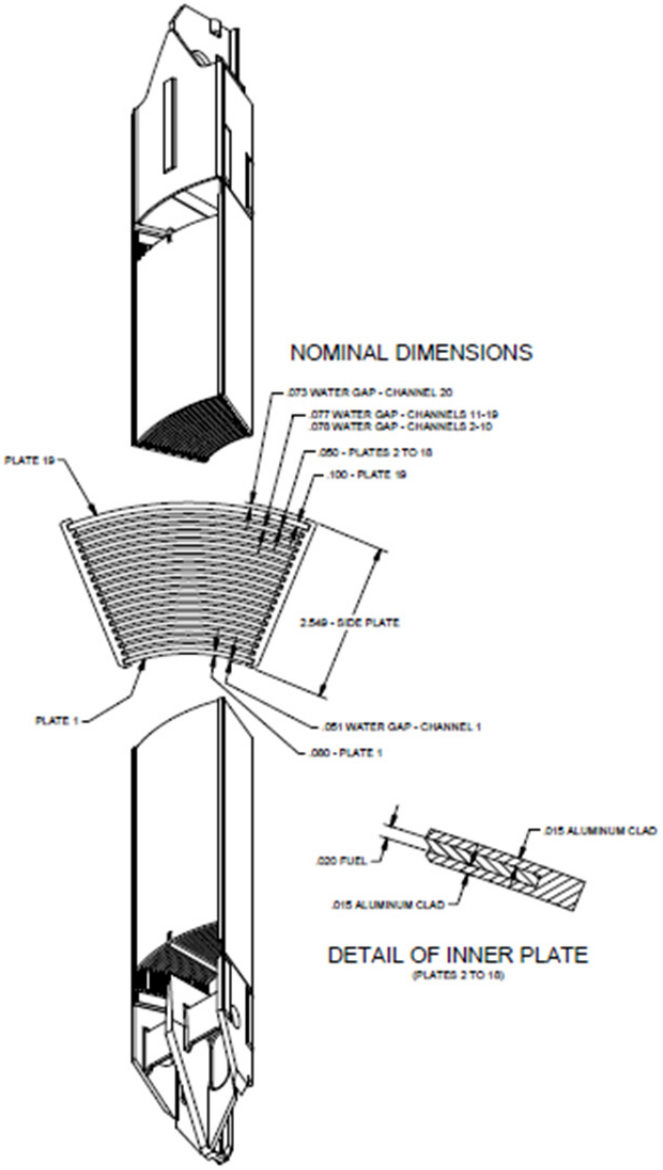

Figure 3. A schematic of an ATR nuclear fuel element [6-10]

The four ATR fuel element types approved for use are designated XA/7F, 7NB, YA, and YA-M. They are all versions of the zone-loaded fuel element design and are identically constructed, varying only in the content of the fuel matrix and boron burnable poison loading.

All ATR fuel elements are fabricated with thicker cladding on Plates 1 and 19. The two outermost fuel plates (1 and 19) of each element are designed with extra thick clad to withstand the greater differential pressure resulting from variability of the coolant channels formed by the outer fuel plates and the adjacent beryllium reflector block, flux trap baffle, and neck shim housing (IDO-17021-1). Damage to the structural components (such as the upper and lower adapters), side plates, and exposed surfaces of Plates 1 or 19 is anticipated during fuel element insertion and removal in the core, transfer cans, and storage locations. Plates 1 and 19 are designed to protect the fuel meat from minor damage. The general schematic of the ATR core fuel positions is presented in Figure 4 below.

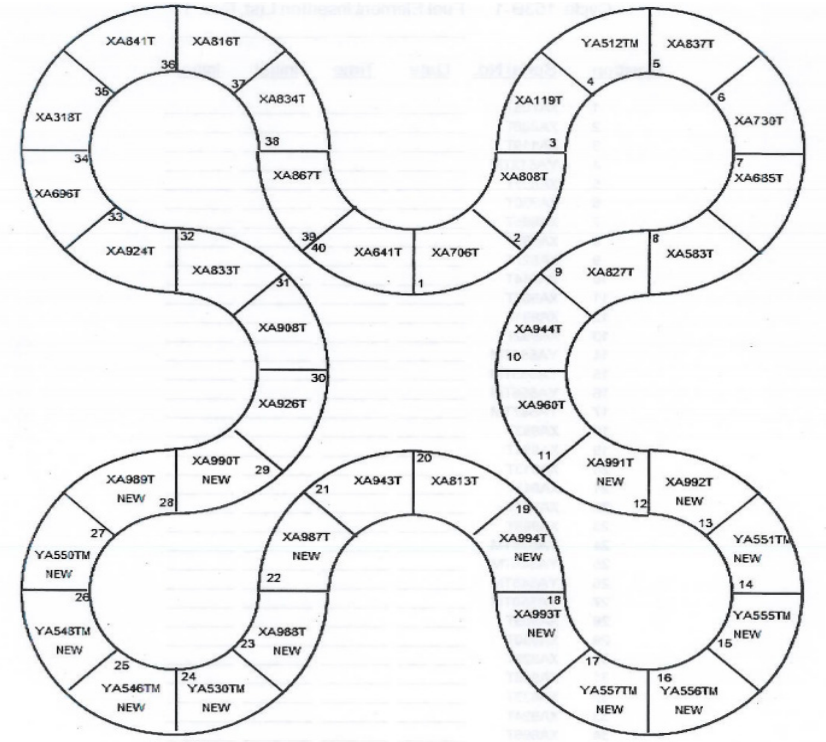

Figure 4. General configuration of the fuel elements in INL Advanced Test Reactor [9] (This core loading corresponds to fuel cycle 153B-1 studied in this report.)

YA type fuel elements were initially specified as “special non-fueled plate 19 XA/7F fuel elements” in 1975. YA fuel elements are identical to standard XA/7F fuel elements, except that plate 19 contains no uranium fuel or burnable boron material. YA fuel elements were originally fabricated for use in core locations adjacent to cracked beryllium reflector block locations, when lobe power was planned to be greater than 48 MW. In several of the early ATR core configurations, cracks developed in the beryllium reflector block in the high neutron fluence region adjacent to the fuel elements, and in some cases beryllium material spalled from the crack, at the A and E ligaments between the outer shim control cylinders and the adjacent fuel elements, see Figure 3. The reactor safety concern was that the spalled beryllium could block the coolant flow in channel 20 on the outer surface of plate 19, resulting in “hot spots” and potential damage to a fueled plate 19.

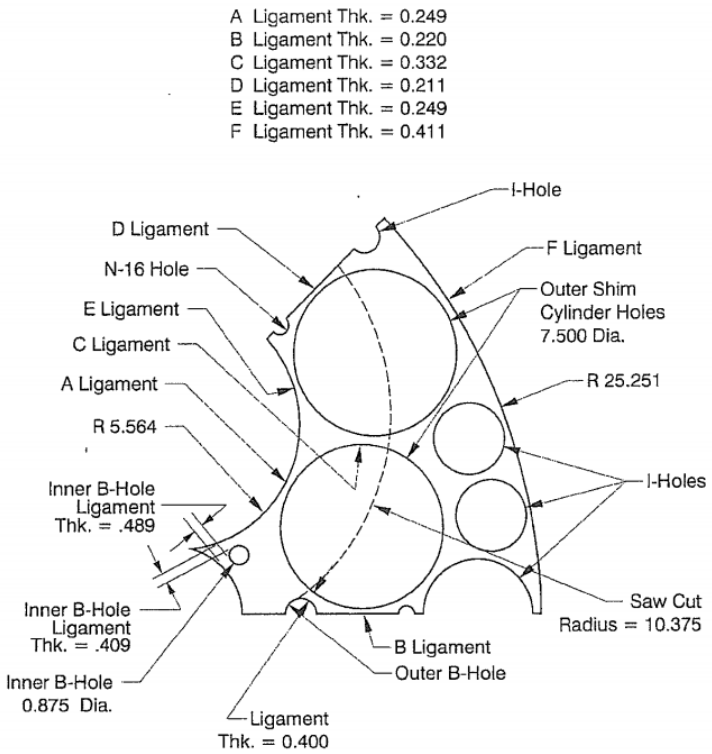

Figure 5. ATR beryllium reflector block ligaments [10]

Another effect of beryllium reflector block aging is swelling of the beryllium, associated with the accumulation of the gaseous products of the beryllium nuclear transmutation reactions – He-4; He-3; and Tritium. In combination with the swelling and bowing of the flux traps, this can result in narrower fuel locations, which makes removal of standard fuel elements more difficult. The fuel element side plate can bind or drag against the flux trap and the beryllium reflector block. YA-M fuel elements are modified YA fuel element with 15 mils machined off the plate 19 edge of the side plates, or in other words, coolant channel 20 is 15 mils narrower on the YA-M fuel elements compared to standard fuel elements, which allows the YA-M fuel elements to be inserted and removed from narrow fuel positions more easily. The 0.073 in. (73 mils) width of coolant channel 20 on a standard fuel element is reduced to 0.058 in. (58 mils) on a YA-M fuel element. The first YA-M fuel element was fabricated in FY-1993. (See Facility Change Form FCF-7.2.1-3 / ECF-3171)

The documented analyses for both the YA and YA-M fuel elements evaluated the structural strength of the aluminum EE plate, the thermal hydraulic effects of a blocked coolant channel 20, and the power density distribution of design basis lobe power with a non-fueled plate 19. The analyzed design basis conditions resulted in acceptable flow, thermal hydraulic, and power density conditions for the adjacent fueled plate 18 and all other fuel plates in YA or YA-M fuel elements.

1.2 ATR Beryllium Reflector Block Modifications

Operating experience with the first two ATR beryllium reflector blocks led to incorporation of horizontal saw cuts in the beryllium blocks of the third and all subsequent beryllium reflector blocks to delay buildup of internal stresses. Axial locations of these saw cuts are shown in Figure 6. Figure 5 shows the radial location of the saw cuts in relation to the A and E ligaments. The saw cuts limit initial cracking in the A and E ligaments to the saw cut segment in which the crack starts.

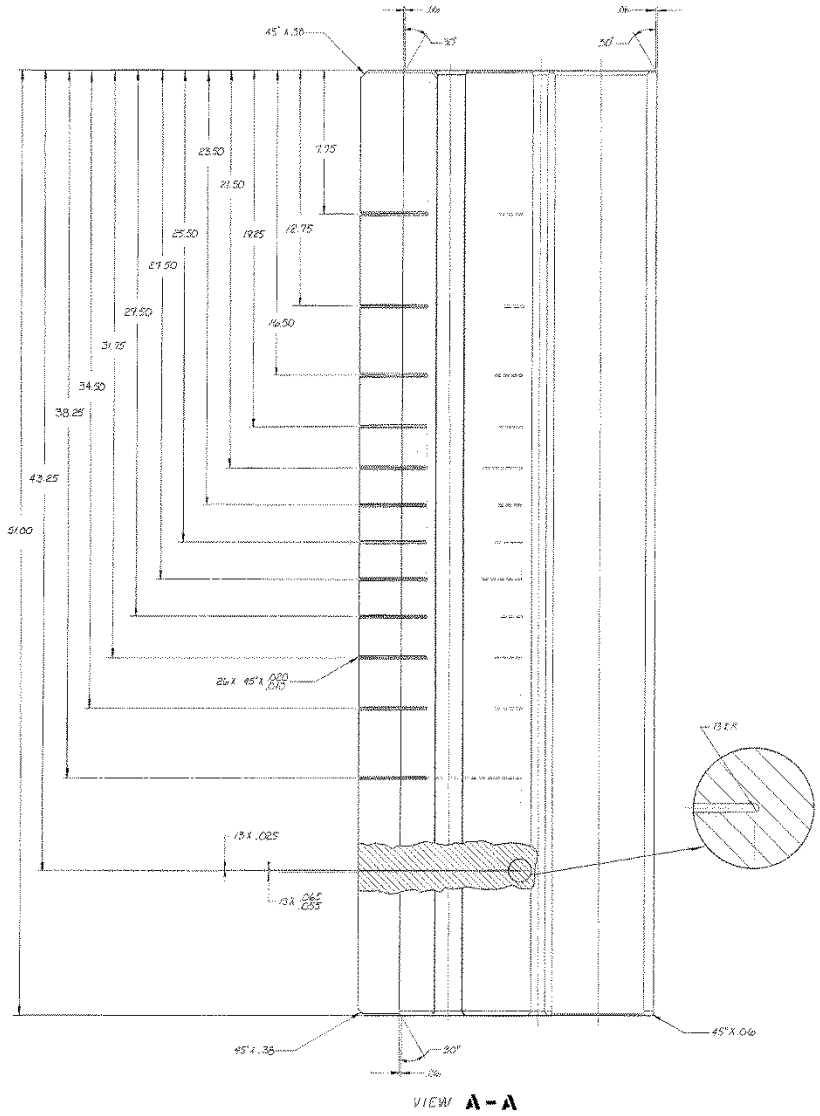

Figure 6. INL drawing DWG 419609 illustrating the geometry and arresting horizontal saw cuts of the beryllium reflector block(s) installed at ATR.

1.3 Potential Contributors to the Pitting Degradation

Some of the effects of corrosion and its mitigation were described earlier by Shaber and Hofman [11]. Previous INL contracts with BWXT procured the fabrication of 175 YA-M fuel elements between 2002 and 2005. Nearly all of these YA-M fuel elements were routinely loaded, inspected, and recycled through numerous ATR core loadings. Once the desired burnup was achieved, the upper and lower adapters were removed, and these spent nuclear fuel elements were shipped to another facility for long term storage and disposal.

Eleven of these remaining recycled YA-M fuel elements, as mentioned in this evaluation, have visible pitting degradation on the exterior of plate 19.

ATR Fuel Management had previously released for use the last remaining eight new YA-M fuel elements that were fabricated in 2005 (YA558TM, YA559TM, YA560TM, YA561TM, YA562TM, YA563TM, YA564TM, and YA565TM). These fuel elements were fabricated, inspected, and certified to meet the requirements for ATR fuel elements as specified in specification IN-F-9A-ATR and drawing 405400 (minor deviations on these fuel elements were identified and accepted using approved procedures). After pitting degradation was discovered during the post-cycle visual inspection, on the eight new YA-M fuel elements that had been loaded in the core for PALM cycle 153B-1, the new YA-M fuel elements remaining in inventory were evaluated prior to use. There are no known non-conformances related to these new YA-M fuel elements that would prevent them from being approved for loading in PALM cycles or any other operating cycle.

More recent INL contracts with BWXT procured additional thirty-six YA-M fuel elements to be fabricated and delivered in 2013 and 2014. ATR Fuel Management had released eight new YA-M fuel elements that were fabricated in 2013. These fuel elements were also fabricated, inspected, and certified to meet the requirements for ATR fuel element specification and drawing (minor deviations on these fuel elements were identified and accepted using approved procedures). These new YA-M fuel elements, fabricated in 2013, were released to maximize the flexibility of YA-M fuel elements approved and released for loading in the 156A-1 PALM cycle. There is no known material differences between the YA-M fuel elements fabricated in 2005 and 2013. Either year of fabrication should have produced equivalent fuel elements.

1.4 ATR Design and Operations

ATR is designed to operate at 250 Megawatts (MW) thermal, but for many years has typically operated at 110 MW (about 44% of rated power). ATR is not required to operate with a flat radial power distribution. ATR is designed to operate with a flux tilt or power ratio across the core as high as 3:1. Cycle 153B-1 had a power ratio of nearly 3:1, with the power level in the southeast (SE) lobe at 55 MW and the power levels in the northeast (NE) and northwest (NW) lobes at 20 MW. The 55 MW in the SE lobe was the highest lobe power for an ATR lobe in many years. The coolant inlet temperature is 125°F and the coolant outlet temperature is 170°F at maximum power such as the SE lobe. Lower lobe powers will produce a smaller differential temperature rise across the core.

Under current practice, the ATR core is loaded with a mixture of both new un-irradiated and recycled irradiated fuel element assemblies for every operating cycle. Cycle length varies between 1 and 60 days. All fuel elements are inspected prior to insertion into the ATR core for each new operating cycle, and all fuel elements are removed from the core after each operating cycle [1-5].

ATR performs a core internal change-out (CIC) every 7-10 years. All of the core components in the core reflector tank are removed and replaced with new components. Historically, ATR PALM cycles were performed in the first few years after CICs were completed while the core components were relatively new and had not begun to swell, bow, or show other signs of aging. PALM cycle 153B-1 and eight additional PALM cycles were planned to be completed prior to the next scheduled CIC in 2020. Because these PALM cycles have been scheduled late in the CIC life cycle, the effects of aging on the core components will be the greatest. Another factor to consider for these PALM cycles is that the requested power levels in the PALM lobes are higher than power levels in previous PALM cycles 20 years earlier. These factors may be contributing to the observed pitting degradation.

The core loading for Cycle 153B-1 consisted of eight (8) new YA-M fuel elements, one (1) recycled YA-M fuel element, eight (8) new XA/7F fuel elements, and twenty-three (23) recycled XA/7F fuel elements (see NE-19-13, Rev. 1, Ref. 5, also see Figure 4 above).

Eight new YA-M fuel elements (YA530TM, YA546TM, YA548TM, YA550TM, YA551TM, YA555TM, YA556TM, and YA557TM) were loaded into the ATR core for cycle 153B-1. Four of these YA-M fuel elements were loaded into both the southeast and southwest lobes adjacent to the two PALM transient experiments. These YA-M fuel elements met all fabrication and inspection requirements, as defined by the ATR fuel element specification and drawings (minor deviations on these fuel elements were identified and accepted using approved procedures).

The one recycled YA-M fuel element YA512TM was loaded into the low power northeast (NE) lobe during PALM cycle 153B-1 and showed no signs of pitting degradation. YA512TM was never loaded in a high power lobe during any PALM cycle. YA512TM achieved the desired burnup and was placed on the 2014 fuel element cut and ship list as spent nuclear fuel.

1.5 Literature Search

A literature search on corrosion of nuclear reactor fuel cladding reveals numerous articles, publications, and documents that identified cladding corrosion that occurred over ten (10) or more years, see Figure 7. Some of these publications have identified the onset of corrosion/erosion in a little as 60 days. No publications were identified, which reported significant loss of cladding material in a period as short as 14 days.

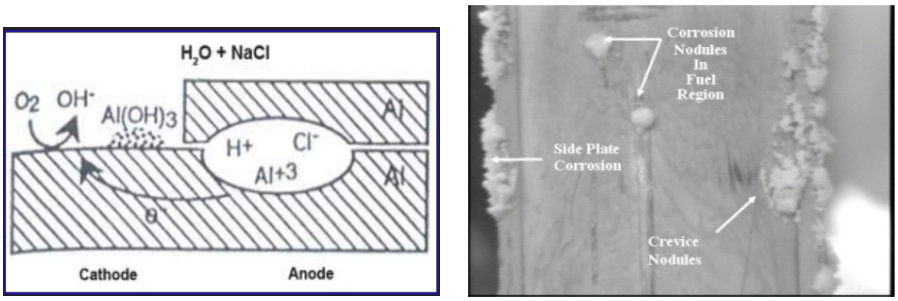

Figure 7. Schematic of crevice corrosion,[1] crevice corrosion at side plates in wet storage.[2]

Corrosion was usually described as a buildup of corrosion products on the surface of the fuel cladding.

Pitting was usually limited to a single or a few isolated locations where material loss produced a depression in the fuel cladding.

Nothing was found in the literature search that reported several thousands of pits forming over large areas in a very short period of time.

1.6 Inspection and Documentation of Fuel Elements Defects

Irradiated ATR fuel elements with discoloration, scratches, gouges and other surface indications, or debris in the coolant channels are identified during the visual inspections performed after the fuel elements have been removed from the core. Typically, 10 to 20 percent of the fuel elements removed from the core will be identified with defects after an operating cycle. The ATR Canal Operators performing the inspections are required to record all observed defects and anomalies on the inspection record sheet. Any defect or anomaly, which in the judgment of the operator is not acceptable, is identified as a deficiency on the inspection record sheet and a nonconformance report (NCR) is generated. Any fuel element with an open NCR against it is not approved for loading into the ATR core. The following sections describe all of the pitted YA fuel elements identified during subsequent visual inspections.

1.7 Results of Coolant Channel and Oxide Measurements on Pitted YA-M Fuel Elements

The ATR Upgraded Final Safety Analysis Report (UFSAR, SAR-153) Section 4.2.1.8.1, Fuel Elements states the following:

> *As soon as practicable following discharge from the reactor, the thickness of the corrosion-product film on selected fuel elements is measured to ensure that the film on recycled elements does not exceed the limit of Section 4.2.1.1. The oxide data are evaluated to provide assurance the limit will not be exceeded. Cooling channel thickness measurements are also made on selected fuel elements to ensure that recycled elements are mechanically sound. The channel thickness measurement data are evaluated for indications of anomalies that indicate unacceptable fuel element performance. Additionally, all recycled fuel elements are visually inspected prior to reinsertion in the reactor.*

All of the fuel elements are visually inspected prior to loading in the core and after being removed from the core. Prior to every ATR operating cycle, one fuel element in the core loading, which is expected to be subjected to the most severe operating conditions, is selected for post-cycle surveillance. After being removed from the core, following power operations, the outer four coolant channels on the selected fuel element are measured and evaluated to determine if any unacceptable reduction of the coolant channel dimensions has occurred. Oxide layer measurements are performed on the exposed surface of plate 19 and the side plates on the selected fuel element. Acceptable coolant channel and oxide measurements on the selected fuel element provided sufficient data to justify recycle use of all 40 fuel elements from the core loading.

Several of the YA fuel elements from PALM cycles 153B-1 and 156A-1 were evaluated in the canal for coolant channel and oxide measurements, which showed no reduction in the coolant channel dimensions and typical oxide layer thickness on all fuel elements examined since the pitting degradation first occurred, Figure 8.

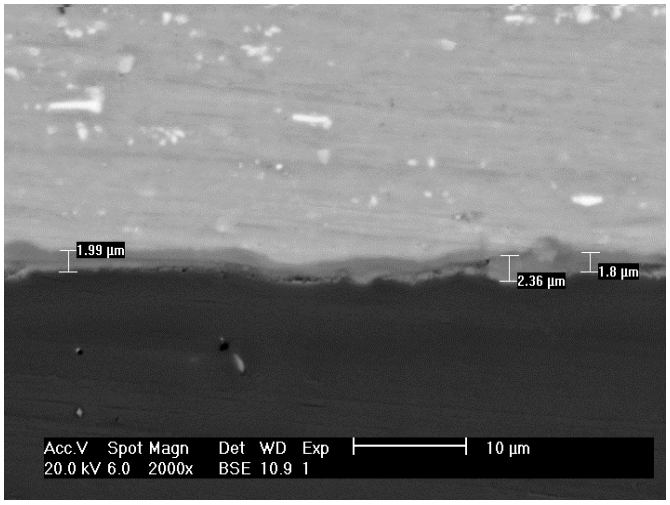

Figure 8. Protective layer of boehmite on the surface of aluminum alloy 6061 [15]

A protective layer of boehmite is of the order of 0.06 to 0.3 mils (1.5µm to 7.6µm) thick [16]; a typical view of 0.08 mil (2µm) the protective boehmite film is presented in Figure 8, see above.

ATR Fuel Management requested coolant channel and oxide measurements on several of the YA-M fuel elements from PALM cycle 153B-1. The channel measurement probe is a flat metal plate with an eddy current sensor between two leaf springs to measure the distance between the fuel plates within the fuel element. The channel probe is very sensitive to any reduction in the coolant channel dimensions. The coolant channel measurements taken in the ATR canal are consistent with coolant channel measurements taken by BWXT during fuel element fabrication. The concern was that the pitting degradation may have reduced the dimensions of coolant channel 19 between fuel plate 18 and aluminum dummy plate 19. The requested coolant channel and oxide measurements were completed on pitted YA-M fuel elements YA530TM, YA548TM, and YA546TM on August 27 and 28, 2013. ATR Fuel Management and Quality Assurance personnel were present when the measurements were taken, and all of the measurements were normal and met acceptance requirements. There was no reduction in the coolant channel dimensions. There was a slight increase in the oxide layer, which is normal for ATR fuel elements after being loaded in the ATR core for an operating cycle [1-10].

For the YA-M fuel elements, plate 19 does not contain fuel, but there is a concern that the pitting on plate 19 could affect flow or heat transfer from an adjacent fuel plate (plate 18). Coolant channel and oxide layer measurements were performed on several of the YA-M fuel elements with pitting degradation. The coolant channel dimensions were not affected. The pitting has obviously removed aluminum material from plate 19, which may increase flow surrounding plate 19 on these YA-M fuel elements. Several inches at the top and bottom of each plate 19 was unaffected by the pitting, the flow into and out of channels 19 and 20 should be controlled near normal values. Therefore, flow perturbations affecting fueled plate 18 (or any other fueled plate) should be minimal. Channels 19 and 20 are most likely to be affected, in that they may see an increase in flow, not a decrease in flow. An increase in flow through a coolant channel is not a reactor safety concern.

ATR fuel elements may be power restricted for nonconforming narrow coolant channels. There is no restriction for oversize channels. Based upon the measurements completed to date, there has been no measureable reduction of the fuel element coolant channel dimensions, therefore no basis exists to power restrict any of these YA-M fuel elements.

1.8 Extent of the Condition and Previous PALM Cycle 150A-1

After the eight YA-M type fuel elements were identified with significant pitting degradation after cycle 153B-1, all of the irradiated YA-M fuel elements in the ATR Canal were visually inspected to determine if any other fuel elements had similar pitting degradation. In addition to the eight YA-M fuel elements from PALM cycle 153B-1, three other YA-M fuel elements were identified with similar, but less significant, pitting degradation on aluminum plate 19 (YA438TM, YA469TM, and YA529TM). All three of these YA-M fuel elements were loaded in the previous PALM cycle 150A-1, which operated a peak power of 45 MW in the SW lobe.

YA438TM was loaded as a new fuel element in PALM cycle 150A-1. YA438TM was inspected and reported to have some pitting degradation after irradiation. No NCR was generated against this fuel element. YA438TM was selected for loading in cycle 154B-1 as a recycled fuel element. The element was inspected prior to loading and was evaluated, by the ATR Canal Operator performing the inspection, as acceptable for loading. The post-cycle inspection of YA438TM was completed after cycle 154B-1, and the ATR Canal Operators reported white corrosion deposits on plate 19 and the side plates. There was no pitting degradation on YA438TM. ATR Fuel Management requested coolant channel measurements and oxide measurements on YA438TM. The coolant channel and oxide measurements on YA438TM were acceptable. YA438TM achieved the desired burnup and was placed on the 2015 fuel element cut and ship list.

YA469TM was loaded as a new fuel element in PALM cycle 150A-1, and loaded as a recycled fuel element in cycle 151B-1. Pitting degradation was identified on fuel element YA469TM during extent of condition visual inspections completed after PALM cycle 153B-1.

YA529TM was loaded as a new fuel element in PALM cycle 150A-1, and loaded as a recycled fuel element in cycle 152B-1. Pitting degradation was identified on fuel element YA529TM during extent of condition visual inspections completed after PALM cycle 153B-1.

Because the degradation was limited to the aluminum plate 19, NCRs were never generated for these fuel elements, or the NCRs against these YA-M fuel elements were dispositioned to "use-as-is," and the fuel elements were approved for use as recycled fuel elements in subsequent core loadings. An evaluation was completed that determined the observed pitting degradation was not detrimental to the neutronics, thermos-hydraulics, or structural properties of the ATR core or adjacent fuel elements or fuel plates, and were acceptable for unrestricted use in future operating cycles. (TEV-2090)

1.9 Subsequent Palm Cycle 156A-1

The next scheduled PALM cycle was cycle 156A-1 which was completed in April 2014. The requested power levels in cycle 156A-1 were very similar to the power levels for PALM cycle 153B-1 when the pitting degradation was first observed.

ATR PALM cycle 156A-1 was a 14-day operating cycle with similar core loading, power levels, and operating conditions as PALM cycle 153B-1. All of the YA-M fuel elements loaded in the core for PALM cycle 153B-1were fabricated in 2005. PALM cycle 156A-1 had a mix of eight YA-M fuel elements that were fabricated in 2005 and 2013 loaded in the core. Four YA-M fuel elements were loaded in both the SW and SE lobes in an alternating pattern that placed fuel elements fabricated in 2005 adjacent to fuel elements fabricated in 2013, to ensure that all fuel elements would be exposed to the same operating conditions. Inspections completed after the operating cycle indicated that all eight of the YA-M type fuel elements loaded in the core had similar pitting degradation on the non-fueled EE plate 19. The pitting degradation was not limited to a fabrication issue related to the YA-M fuel elements fabricated in 2005.

1.10 Acceptance Criteria for ATR YA or YA-M Fuel Elements

ATR YA and YA-M fuel elements have no fuel loaded in plate 19, which is an aluminum alloy plate. Therefore, surface defects such as pits, dents, scratches, gouges, or other surface defects to plate 19 on a YA or YA-M fuel element cannot result in damage to a fueled plate. Surface defects on plate 19 of YA and YA-M fuel elements, which reduce the coolant channel measurement of channel 19 to less than approved minimum values, are not acceptable. Pits or scratches to the exterior surface of plate 19 cannot reduce the dimensions of coolant channel 19 on the interior surface of plate 19. A significant dent to the exterior surface of plate 19 or buildup of corrosion deposits on the interior surface of plate 19 could reduce the dimensions of coolant channel 19 to unacceptable values. Satisfactory completion of procedure to measure the fuel element coolant channel is sufficient to verify coolant channel 19 dimensions have not closed to unacceptable dimensions. Pits, dents, scratches, gouges, or other surface defects to plate 19 of a YA or YA-M fuel element, which do not reduce the coolant channel 19 dimensions are not limited in depth, size, or number.

1.11 Further Evaluations

The pitting degradation reported to date appears to be a combination of corrosion and flow erosion. The lack of pitting degradation in the top and bottom 4 inches of plate 19 appeared to indicate that the neutron flux or gamma ray heating from the sinusoidal axial power distribution, from adjacent fuel plates, may have contributed to the pitting degradation of non-fueled plate 19. Multiple factors were suggested as possible contributors to the observed pitting degradation on YA-M fuel elements, including changes in the fabrication or cleaning methods used by BWXT, changes in ATR primary coolant or canal water chemistry, higher lobe power levels in recent PALM cycles, more suspended solids in the primary coolant when the third primary coolant pump was started for PALM cycles, etc. None of these have been definitively identified as a cause or even as a contributor to the observed pitting degradation.

The further evaluations became a process of elimination. Each possible contributor was identified and evaluated. Suggestions were made to eliminate or reduce possible risks when practical, but most were evaluated as negligible or minor contributors, and were not a significant concern.

1.12 ATR Water Chemistry Evaluation

ATR primary coolant system and canal water chemistry sample analytical results were reviewed to determine if there had been any unusual transients in the water chemistry that may have contributed to the observed pitting degradation. There were no abnormal water chemistry transients.

1.13 Microscopic Evaluation of EE Plates

Numerous microscopic examinations were performed on the EE plate aluminum samples provided by BWXT. Similar microscopic examinations were performed on the aluminum end croppings of fuel plates to determine the effect of the differences in the fabrication process on the aluminum microstructure. The microscopic examination identified “large, sharp” silicon dioxide (silica) clumps that may contribute to the pitting degradation as a nucleation site, but cannot explain the observed pitting phenomenon on only the YA-M elements loaded in the core.

1.14 Thermal-Hydraulics Evaluation

A thermo-hydraulics simulation of the flow phenomena in the cooling channels adjacent to the YA-type fuel elements and the beryllium reflector blocks has never been conducted. In particular, it was not established what role, if any, the 13 horizontal cuts (chamfers) play in creating of potential turbulence in the flow. In turn, these peculiarities in the flow structure could exert a certain influence on the observed corrosion/erosion phenomena.

In addition to a base case to establish the basic phenomena in the cooling channel, a parametric case was explored in which the size of the chamfers of the horizontal cuts was altered. This was done to observe how a change in flow channel geometry would affect coolant flow.

These results are described below in Section 4.

1.15 Organization of the Report

This report is organized as follows. In Section 2, different metallurgical factors are presented that may have contributed to both types of corrosion/erosion accompanied by de-alloying. Thermo-mechanical treatments of fuel plates and dummy plates are compared, and conclusions are made on the need to modify treatment of the plate of YA (dummy) type. In Section 3 calculations of the neutron flux for different types of plate are presented (in the approximation of 49 and 6 energy groups) using HELIOS and MCNP software are presented. Section 4 contains the results of thermo-hydraulic modeling that shed light upon both types of observed erosion phenomena. In Section 5 conclusions and recommendations are made to alleviate, or exclude altogether similar erosion events in the future. Finally, references are presented in Section 6.

2. ANALYSIS OF THERMO-MECHANICAL PROCESSING OPERATIONS USED FOR MANUFACTURING 6061-O, 6061-T6, AND DUMMY SHEET

2.1 Aluminum Plate EE Fabrication Evaluation

The cause of observed pitting degradation on ATR YA-M fuel elements loaded in high power lobes during high power PALM cycles has been identified. A more detailed technical analysis follows in the subsequent sections of this report. The dummy plate subjected to corrosion/erosion was photographed inside the canal, and erosion sites are clearly visible in both photographs, see Figure 1. The dissolution of

the plate material was taking place accompanied by the subsequent leaching out of erosion sites. The direction conicides with that of the coolant flow. Thus, one can speak about so-called "flow-assisted erosion" (FAC), possibly facilitated by the processes of erosion and de-alloying.

Yet another, very different type of erosion was also observed, see Figure 2. It is clear that some dissolution of the plate material was taking place accompanied by the subsequent leaching out of erosion sites. The direction conicides with that of the coolant flow.

This is typical of the pitting erosion process, possibly accompanied by some crevice and/or erosion corrosion. The general schematic of the crevice corrosion is presented in Figure 7, see above.

The directional character of erosion is clearly seen from Figures 1 and 2. The erosion is mostly localized in the center of the plate.

The authors have examined a significant body of past work describing different kinds of corrosion/erosion events with this type of fuel plates made of AA6061 [13-30] over several decades of operation of similar reactors. In many cases, corrosion of the crevice and/or pitting type takes place in wet storage of spent nuclear fuel plates in the pool over many years or decades.

It is important to emphasize[1] that the oxide film growth on the surface of a fuel plate in working conditions is a normal phenomenon. Many of aluminum oxides are characterized by protective properties and passivate the metallic surface against further corrosion.[9] These are, for example, γ–Al_2O_3 (possessing the structure of defect spinel, with vacancies distributed on the cation sublattice only[1]), or γ-AlO(OH), the so-called "boehmite," or "pseudo-boehmite" forming between 171°F to 216°F (~77°C and 102°C). [13] The crystalline boehmite modification is actually used as a thin protective layer in many aluminum alloy fuel elements and can be grown on the surface of the plate by "boiling" it at elevated temperature above 216°F (102°C) and pressure below 2,900 psig (20 MPa).[13]

Detailed studies of different aluminum oxides and hydroxides were conducted at Alcoa Inc. and summarized in the now classical Alcoa Technical Paper no. 19 by Wefers and Misra.[9] These researchers have established that mutual transformations of these polytypes obey certain rules of crystallography and the group theory and generally follow 4 distinctive types of transformation cascades,[9] Figure 9:

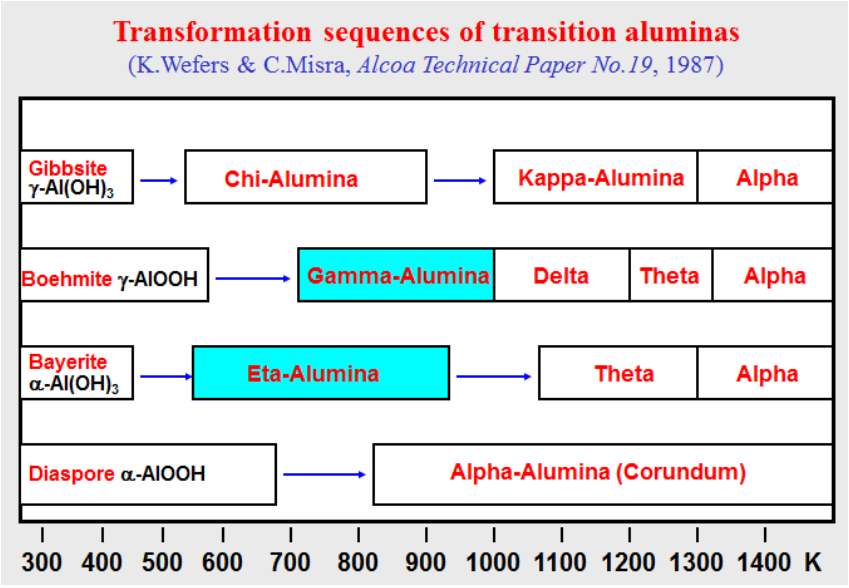

Figure 9. Crystallographic transformation sequences for different alumina polytypic structures.[9]

Corrosion events were observed not only in wet storage of spent nuclear fuel, but also in the working reactors as well. One example is described by Henslee,[21] who discovered that foreign metallic particles

(Pb, Fe, Cr) impregnated into soft aluminum alloy when rolling it to gauge. Any of these elements might have serve as a nucleation site of pitting corrosion. The author of Reference 21 made a conclusion that "the major source of contamination may be due to the fabrication sequence and subsequent material handling."

The **working hypothesis** was that a confluence of factors, - different thermo-mechanical treatment of YA elements and PALM irradiation cycles with increased fluence and the increased coolant fluid velocity (3 PCPs) - might have contributed to the observed erosion event. In this section, only the metallurgical aspects and corresponding remediate actions are described (i.e., recrystallization, microstructure, residual stress etc.), while irradiation and thermo-hydraulics aspects are examined in detail in the subsequent sections.

A contract was placed to have BWXT fabricate aluminum samples of the EE plate 19 of YA fuel elements. The samples were representative of the various steps within the fabrication process for the EE plates on YA fuel elements. The furnished EE plates were examined to identify a possible mechanism for the observed pitting degradation on the YA fuel elements removed from the core after PALM cycles 153B-1 and 156A-1.

The EE plates are processed significantly differently from fuel plates. A fuel plate is hot rolled, cold rolled, annealed twice, and has a 87% reduction in thickness. As opposed to the EE plate which is cold rolled, annealed once, and has a 30% reduction in thickness. The difference in the rolling process resulted in different grain structures, which were not likely to contribute to the observed pitting degradation.

Both fuel plates and EE plates are subjected to a program anneal at 775°F (413°C) for 2.5 hours. The fuel plates were subjected to an additional blister anneal at 900°F (482°C) for 2.5 hours. The higher temperature anneal for fuel plates was expected to produce additional grain growth, which may help prevent corrosion and erosion. A request was submitted and BWXT revised the fabrication process for the EE dummy plates to include an additional blister anneal at 900°F (482°C) for 2.5 hours. The first YA-M fuel elements to be fabricated using the revised process are scheduled to be fabricated in 2017, and are expected to be loaded in the ATR core in 2018, so several years will pass before the effects of the additional blister anneal of the EE plate can be evaluated.

According to the existing specifications, thermo-mechanical treatment of AA6061 aluminum alloy sheet included the following operations:

Based upon the careful inspection of the currently adopted thermo-mechanical treatment for the YA type sheet, it was hypothesized that the metallurgical aspects of erosion of dummy plates might be related to the **excessive residual stress** remaining after just one, relatively low-temperature, program anneal. In principle, there are **two possible sources of stress**: elastically coherent or semi-coherent particles of Mg_2Si; and incomplete recrystallization. Below both factors are considered in detail. If the hypothesis turns out to be true, then a possible remedial action could be taken to eliminate all sources of residual stress via modification of the existing thermo-mechanical treatment. Such a modification was developed in the present report based upon the results of thermodynamic and kinetic modeling mimicking the thermo-mechanical treatment processes, to which the sheet will be subjected.

Recrystallization is an important phenomenon that occurs during hot deformation or upon annealing. For aluminum, it is important to understand the rate of recrystallization when considering processing parameters because overall strength and surface quality need to be tailored to meet end requirements. Recrystallization closely resembles other processes that relieve internal stresses created during deformation such as recovery. Recrystallization is defined as the formation of a new grain structure in a deformed material by the formation and migration of high angle boundaries (misorientations between 10° - 15°) driven by stored energy created during deformation. From this definition of recrystallization, it can be seen that the rate of recrystallization is a function of the stored energy that is created during

deformation by varying processing parameters and heat treatments. Some quantitative data found in the literature[3] is presented in Table 1:

Table 1. The fraction (%) recrystallized of rolled 6061 annealed ingot (thickness reduction 10% to 70%) after 1 h heat treatment at various temperatures 600°F to 1000°F (316 to 538°C).[3]

Thickness Reduction (%)	Annealing Temperature, in °C and in °F								
	316°C	343°C	371°C	399°C	427°C	454°C	482°C	510°C	538°C
	600°F	650°F	700°F	750°F	800°F	850°F	900°F	950°F	1000°F
10.6	0.0	0.0	0.0	2.9	4.3	6.1	6.8	7.6	8.1
22.5	0.0	0.9	6.9	12.8	14.3	19.8	24.3	30.5	39.5
32.4	0.0	3.7	11.4	24.9	32.8	43.8	50.0	62.4	80.7
40.4	11.0	14.0	29.4	36.0	57.9	59.3	71.0	89.8	98.1
50.4	22.3	36.2	40.2	49.3	70.1	73.2	89.2	98.1	100
60.5	40.3	50.3	64.3	75.3	83.4	91.2	95.3	100	100
70.4	61.0	70.3	78.2	82.4	91.4	96.1	99.1	100	100

At BWXT, aluminum plate is annealed for 2 hours at temperature 775°F (413°C) in the case of program anneal, and at temperature 900°F (482°C) – in the case of blister anneal. Comparing these data to the results from Table 1, one can conclude that the probability of achieving incomplete recrystallization in the case of the dummy plate fabrication (only program anneal) is quite substantial.

An example of incomplete recrystallization that may cause residual stresses in alloy micro-structure is presented below.[4] The picture was obtained on a modern Helios PFIB 3D-microscope.[5]

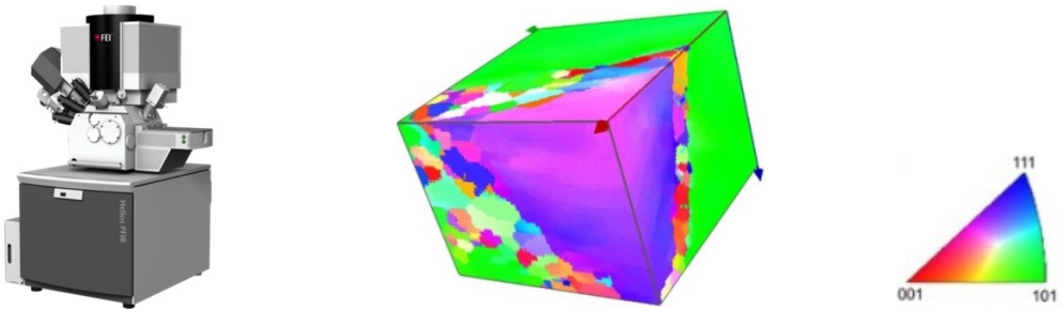

Figure 10. Left: a modern Helios PFIB microscope;[4] Right: 3D-representation of partial recrystallization in Al alloy.[5]

An important thing to keep in mind is that dummy EE plates are subjected to 33% reduction, while the fuel plates – to 70% reduction or greater. It also makes a difference in the degree of recrystallization of these materials in the sense that it is more difficult for dummy plates to achieve the state of complete recrystallization.

Data on different mechanical properties of alloy AA6061 in the T6 and the O tempers is presented in Table 2.

Table 2. Mechanical properties of alloy 6061 in the T6- and the O-tempers; with cold rolling and heat treatment at 413C alloy strength must somewhere in between these two boundaries.[5]
1 ksi = 6.875 mPa.[6]

Temper	UTS (ksi)	YS (ksi)	Elongation, %	Brinell hardness
AA6061-O	18	8	25	30
AA6061-T6	45	40	12	95

The other possible mechanism of aluminum alloy sheet strengthening is by Mg_2Si precipitates (coherent and semi-coherent). The precipitation of the Mg_2Si secondary phase particles ("dispersoids") out of solid solution has been examined in great detail as it allows understanding both the strengthening and corrosion behavior of the alloy AA6061.The initial stage of the formation of Mg_2Si includes the formation of atomic clusters called "Guinier-Preston zones." Then, β"-Mg_2Si forms as coherent Widmanstatten needles in the [100] crystallographic direction. The β" needles transform into semi-coherent β' rods typically rendering a given Al-Mg-Si alloy its maximum strength (they are semi-coherent and the most effective at arresting dislocations motion). At the final stage of this cascade of ageing processes, the rods are transformed into β-Mg_2Si platelets, which represent the true equilibrium phase. Along with forming precipitates, magnesium and silicon also serve the function of solid solution strengtheners. In the O-temper, the equilibrium phase Mg_2Si will be observed, but coherent and semi-coherent particles of Mg_2Si will be absent.

According to References 7, 8, and 9, the precipitation events in the ternary 6xxx alloys represented by the Al–Mg–Si system can be described by the general scheme below:

solid solution → GP → β" → β' →(B')→ β

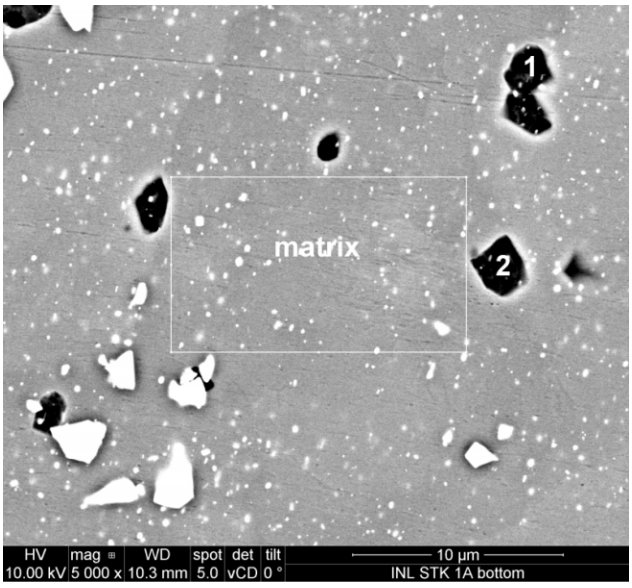

Figure 11. Typical microstructure of AA6061 "dummy" plate: saturated Al-based solid solution, particles of Mg_2Si (dark, 1 and 2), and white particles of Fe-bearing phases such as Al_3Fe, Al_5FeSi, etc. (our data).

According to Figure 11, particles of Mg_2Si, Al_3Fe, Al_5FeSi etc. were found in samples of the dummy sheet. In general, a number of different phases may form in the Al-Mg-Si-Fe system ("mimicking" alloy 6061 to a certain extent), including saturated solid solution (Al), Mg_2Si in different forms, Al_3Fe, Al_5FeSi, Al_8Mg_5, etc. Clearly, this alloy, similar to any industrial alloys, is characterized

by the very considerable complexity. In order to understand thermodynamics and kinetics of different processes associated with its thermo-mechanical treatment, *JMatPro* v. 8.2 (Sente Software, Cambridge, England) was used for the computer modeling simulation of different heat treatments for AA6061 sheet that are presented in the next paragraph.[10]

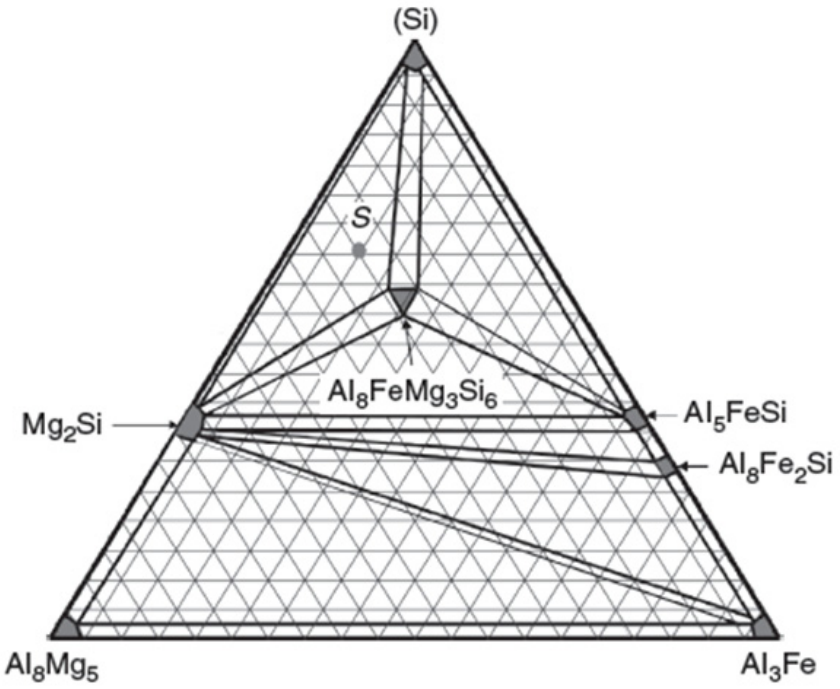

Figure 12. Isothermal cross-section in the Al_8Mg_5 – Al_3Fe – (Si) pseudo-ternary phase diagram illustrating the character of phase equilibria in this complex system and phases that can potentially be present in AA6061.[11]

2.2 Modeling of Mg_xSi_y Precipitation in AA6061 and Residual Alloy Strength

The goal of the 775°F heat treatment is to remove the potential for subsequent formation of the metastable Mg_xSi_y precipitates and, thereby, any potential for particle elastic conjugation with the Al-matrix. Unfortunately, this may well not be the case for the ATR Al alloy. Metastable calculation, with heat treatment at 775°F, clearly shows that there is very significant level of Mg remaining in the Al-matrix as well as a rather significant level of Si. That means there is **a potential for hardening** after the 775°F 2-hour heat treatment.

If there is incomplete re-crystallization and significant levels of internal stress, then the transformation rates would be increased. To what level is difficult to say. However, there would clearly be an increased potential for hardening phases to form during cooling. This may potentially explain the observed pitting degradation.

Figures 13 and 14 represent phase compositions, stable and metastable respectively, for alloy AA6061 as a function of temperature. These Figures are important for evaluating a possibility of metastable precipitates remaining in the (Al)-matrix and, consequently, for creating and retaining a certain level of the residual stress that may contribute to the phenomenon of pitting erosion.

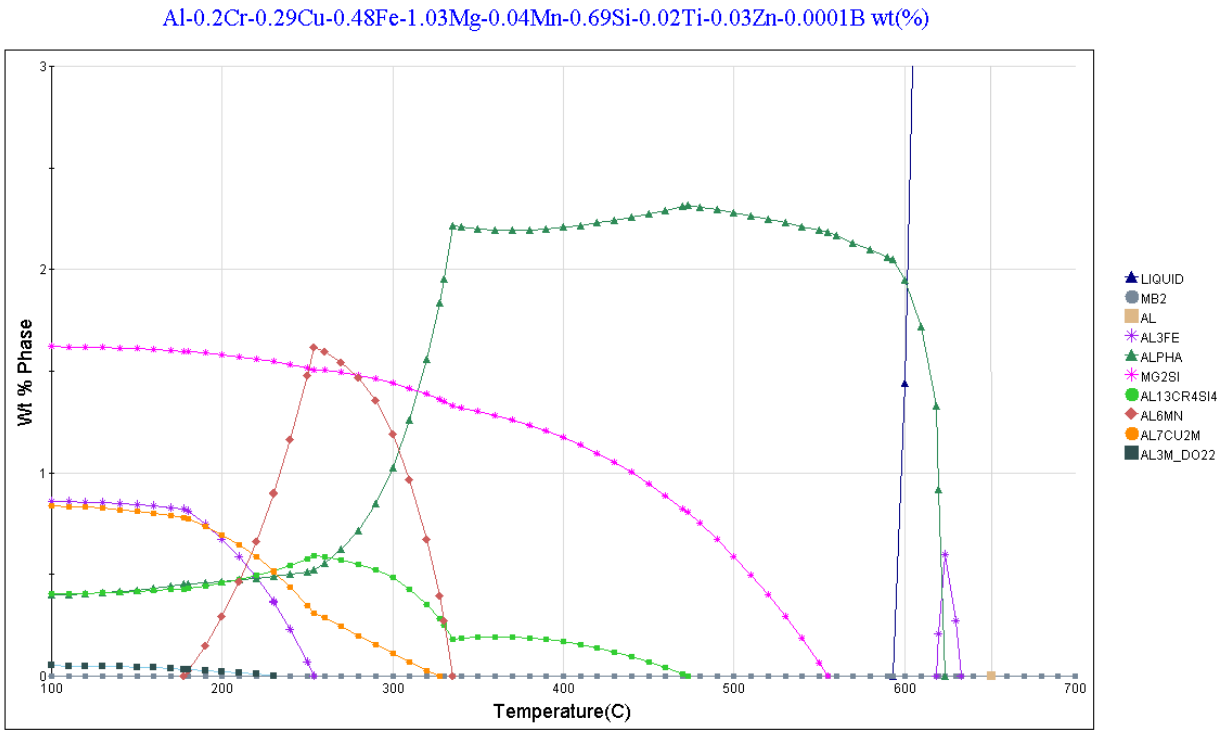

Figure 13. Temperature dependence for equilibrium alloy 6061 phase composition.

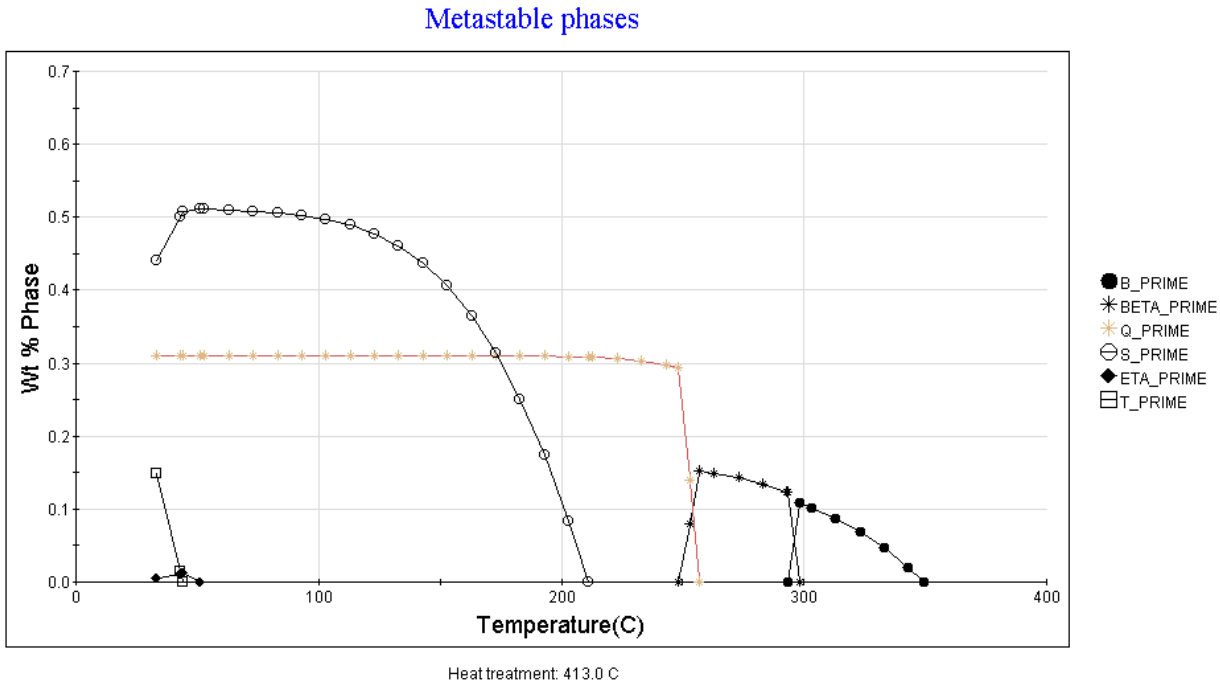

Figure 14. Metastable phases and their weight content as a function of temperature for the preceding heat treatment at 413°C.

Our next goal was to model the kinetics of precipitation of both equilibrium and metastable phases in AA6061 subjected just to thermo-mechanical treatment of reduction by 33% (cold rolling) and subsequent anneal at 413°C for 2 hours. The results are demonstrated in Figure 15.

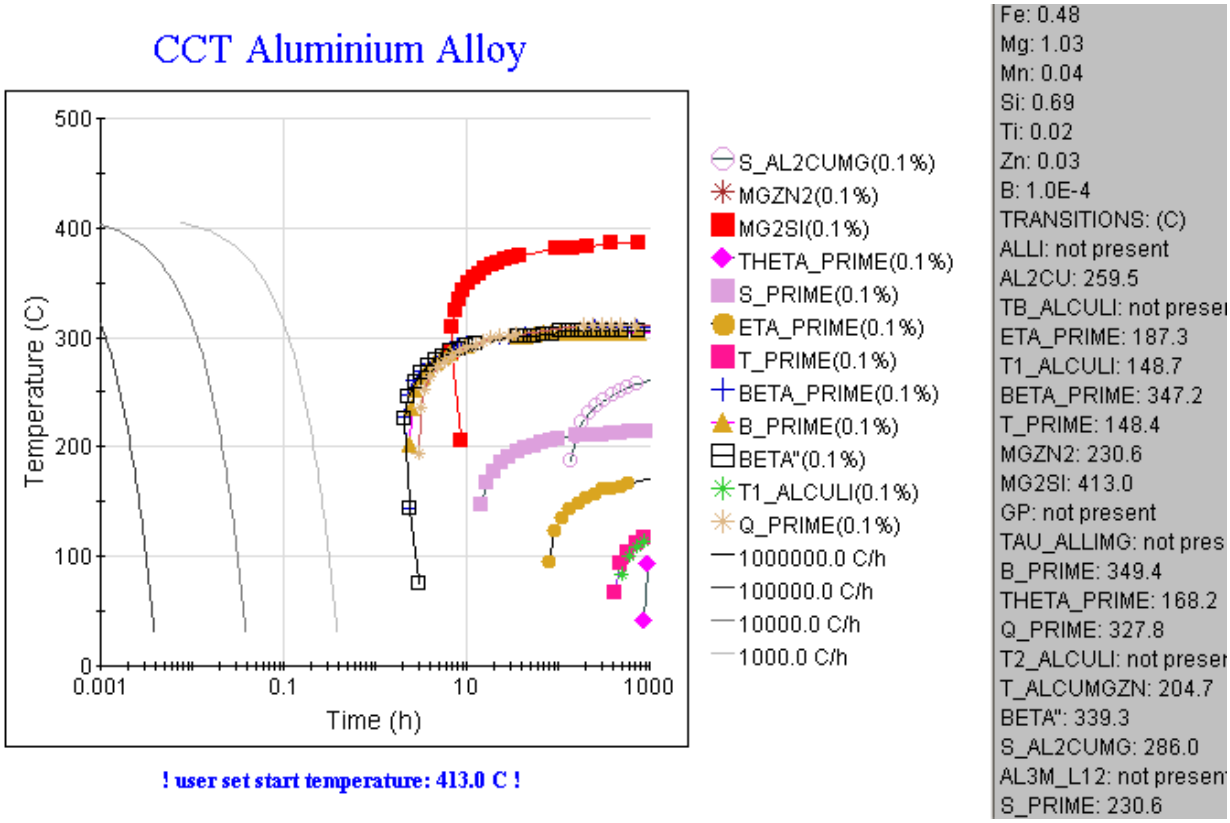

Figure 15. Continuous cooling diagrams from 413°C down to room temperature for different cooling rates, including cooling in the ambient air (1000 C/hour; light grey line).

One can see that the light grey line corresponding to cooling in the air (~1000C/h) is uncomfortably close to the CCT lines for precipitation of different metastable phases such as β' or β". Consequently, additional high temperature anneal seems attractive both from the complete recrystallization and the elimination of metastable phase point of view.

Strength calculations were run (Figure 16), which demonstrated that little hardening was left after 2 hours holding at 413°C (770F). This seems to imply that there is indeed a potential for additional hardening during the cooling process after the 413°C treatment. Next, if "dummy" plate is harder, what could be done to reduce its hardness?

One possible solution to eliminate the flow-assisted erosion problem would be to cold roll, then add blister anneal (2 hours at 900°F), then follow up with program anneal (2 hours at 775°F). Probably it could even be possible to drop temperature of the 2nd anneal down to 700°F. This was suggested to the fuel fabricator, BWXT. The annealing procedures were revised to add the higher temperature blister anneal to the EE plate fabrication procedure.

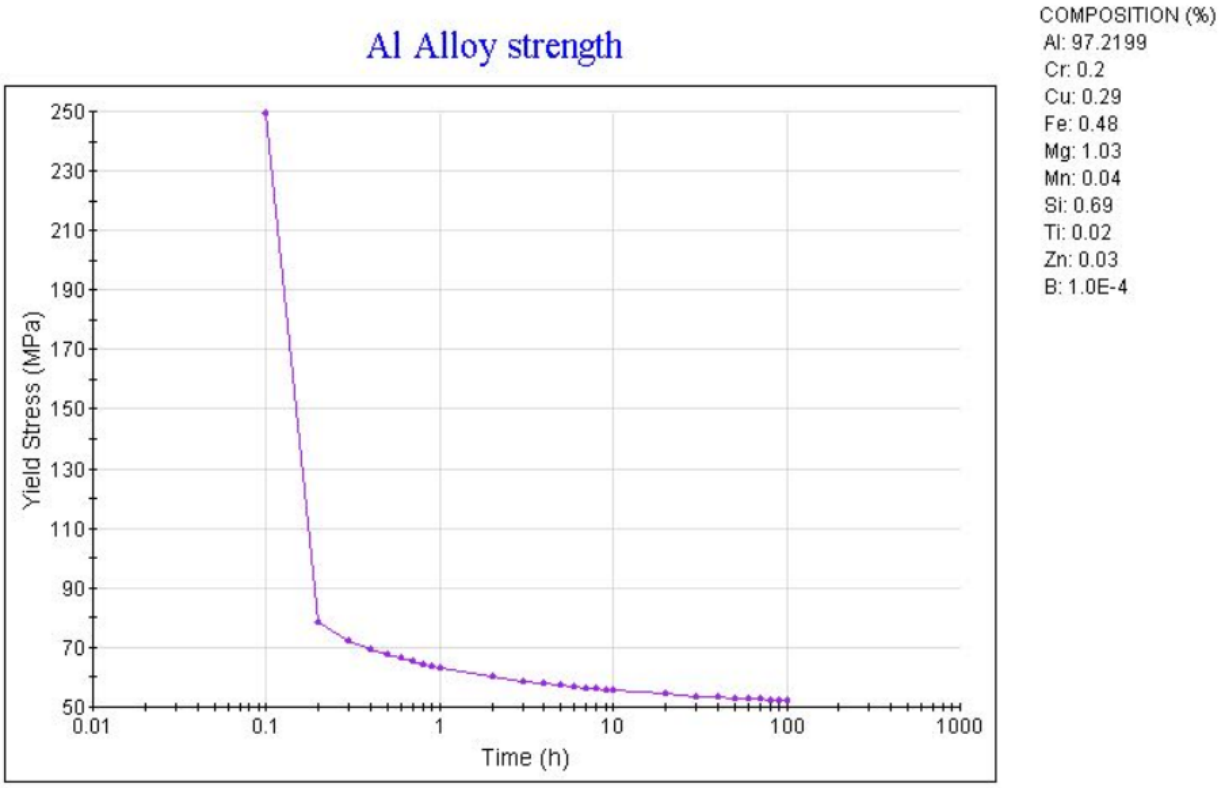

Figure 16. Modeling of residual AA6061 alloy strength: after 2 hours of heat treatment at 413°C sheet still has about 62MPa residual strength. This is higher than 55MPa for AA6061-O. Strength can further increase as a result of natural aging during cooling in the air.

2.3 Corrosion Perspective

Localized corrosion susceptibility of Al alloys is associated with the presence of second-phase particles in the alloy (SPPs)

SPPs in AA6061 can be classified into 2 main kinds: active particles rich in magnesium, silicon and aluminum; and particles with iron, silicon and chromium which show cathodic behavior relative to the aluminum matrix. The behavior of second-phase particles present in aluminum alloys has been studied in low conductivity solutions.

For AA 6061 alloy in aerated high purity water at open circuit potential, it was found that the iron-rich particles act as cathodic sites promoting the oxygen reduction reaction, generating a localized pH increase that provokes aluminum dissolution around the particles.

In AA 6061 alloy, it was found that Mg_2Si particles undergoes selective magnesium dissolution in high purity water (conductivity $\kappa = 0.05$ S/cm; pH = 5.5) – anodic behavior.[12]

The presence of particles with undesirable morphology results in piercing the protective boehmite layer on the 6061 plate surface. This creates local stress concentrators and “local” galvanic couples. Cathodic particles (Al_5FeSi or $Al_3Fe(Cr)$) will dissolve the Al-matrix around them with help of residual stress and break free.

Electrochemical behavior of 2nd-phase particles depends mainly upon the potential difference between the particle and the matrix. SPPs in AA 6061 can be classified into two main kinds: active particles rich in Mg, Si and Al; and particles with Fe, Si and Cr which are cathodic relative to the Al-matrix:

1st type (**cathodic**, will be dissolving and eliminated from the aluminum solid solution matrix): Mg_2Si; Al_8Mg_5; the Q phase $Al_5Cu_2Mg_8Si_6$and its metastable precursor; the S phase, Al_2CuMg, and the T-phase, $Al_2Mg_3Zn_3$

2nd type (**anodic,** particles with Fe, Si, and/or Cr): Al_3Fe; Al_5FeSi, the Cr-bearing alpha-phase. Particles of Al_8Fe_2Si will also be prone to anodic corrosion processes.

Precautions need to be taken to avoid the different kinds of corrosion associated with the heterogeneity of AA6061 ("boehmite treatment" of the surface resulting in the formation of the protective layer of γ-AlO(OH); thickness~2μm). Also, it is recommended to make calculations for solubility of different oxides and hydroxides of aluminum, including Boehmite, at different values of pH and for the temperature range corresponding to the inlet, outlet and intermediate temperatures of the coolant liquid in the primary cooling circuit of the ATR. Indeed, the original results were obtained only for temperature 25°C.

3. NEUTRONICS MODELING WITH "MCNP" AND "HELIOS"

3.1 ATR Fuel Element Neutronics Evaluation

The ATR core is designed to operate at power levels up to 250 MW. Each lobe is designed to operate at 60 MW. YA and YA-M fuel elements were specifically designed to operate in lobes with power levels above 48 MW. Fuel plate 19 is the largest fuel plate in an ATR fuel element, but because of the zone loaded fuel density, plate 19 contains only 52.6 grams of U-235, which means that only the five smallest fuel plates in the fuel element contain less U-235 fuel than plate 19. The fact that the aluminum EE plate on YA and YA-M type fuel elements contains no uranium fuel loaded within the plate, results in a relatively minor shift in the power density, neutron fluence, and fuel plate temperatures, when compared to the standard XA/7F type fuel elements.

The higher reactor power levels associated with high power PALM cycles require three primary coolant pump operation, as opposed to two pump operation for lower power cycles. The higher power of a PALM cycle results in higher coolant temperatures, but that is somewhat offset by higher primary flows through the core. The primary coolant inlet temperature is 125°F, and at 250 MW the coolant outlet temperature is 170°F, with less temperature rise across the core at power levels less than 250 MW. The minor increase in fuel plate and primary coolant temperatures due to the operating conditions during a high power PALM cycle may have contributed to the observed pitting degradation.

In order to obtain the necessary data on the neutron flux distribution along the YA element plate, MCNP and HELIOS modeling was conducted. In turn, this data provides information about the heat flux distribution in the axial direction for the core lobes SW and SE, see Figure 17

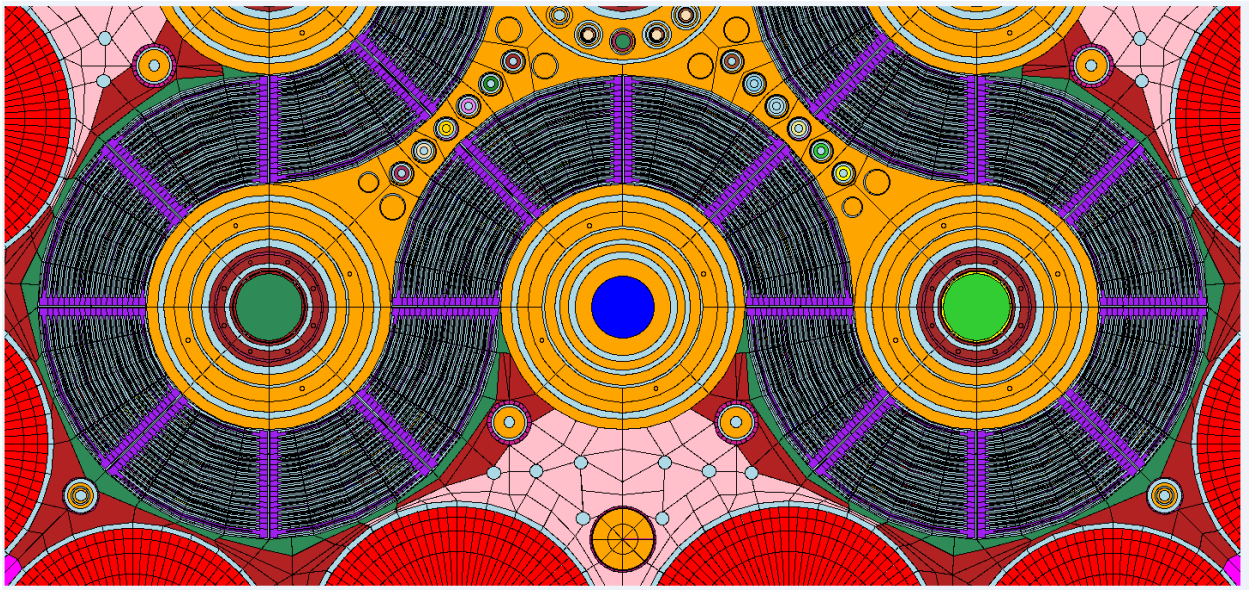

Figure 17. General schematic illustrating positions of the ATR South lobes (cycle 153B).

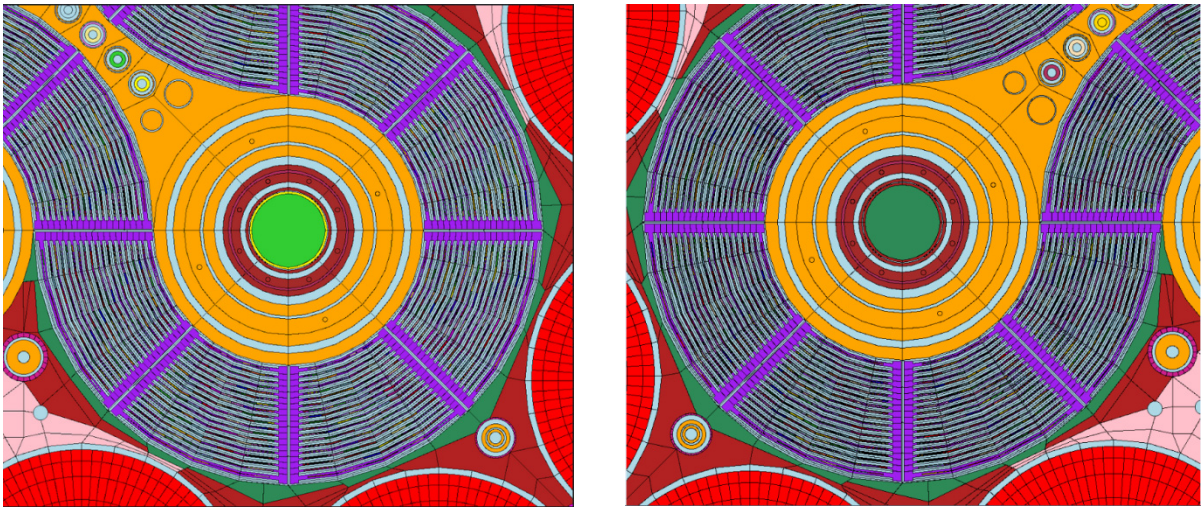

Figure 18. (left) South-East (SE) lobe in ATR cycle 153B; and (right) South West lobe (SE) of ATR in reactor cycle 153B.

As mentioned in Section 1, localized flow assisted axial erosion with possible de-alloying and the formation of pits was observed predominantly in the central part(s) axially of the aluminum dummy plate of YA elements in the SW and SE lobes during the 153B PALM cycle. The initial assumption was that the predominant location of erosion sites in the central parts of the affected plates was the result of residual stresses in the YA fuel plates and the increased levels of axial neutron flux distribution. It is this combination of factors that may have resulted in the observed erosion phenomena. It can be conveniently illustrated by Figure 19.[10]

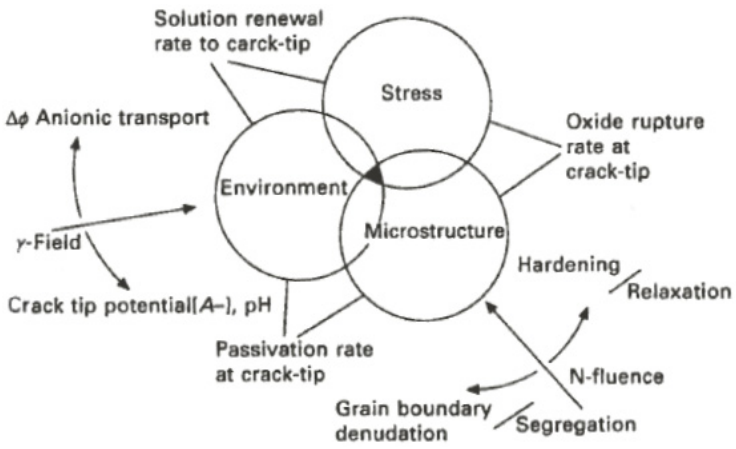

Figure 19. Schematic of primary engineering parameters that affect SCC (Stress Corrosion Cracking) – stress, microstructure, and environment. Radiation affects SCC via segregation, hardening, relaxation, and water radiolysis.[10]

The fuel elements investigated were were loaded in fuel positions 14 – 17 in the SE ATR lobe and fuel positions 24 – 27 in the SW ATR lobe. Neutron flux distribution(s) were calculated in the classical approximation of 6 energy groups using the FMESH4 tally in MCNP. For that goal, the coordinates for the SE and SW lobes were determined to define the appropriate geometric locations within the ATR core. Based upon these results, angles were calculated for each of the fuel elements in the conducted analysis. This was the key parameter for the mesh tally because it helped define the corresponding tally region for each individual fuel element. As a result, a single fuel element axial neutron flux distribution was calculated for the entire length of the active fuel zone. The results of these calculations are presented below.

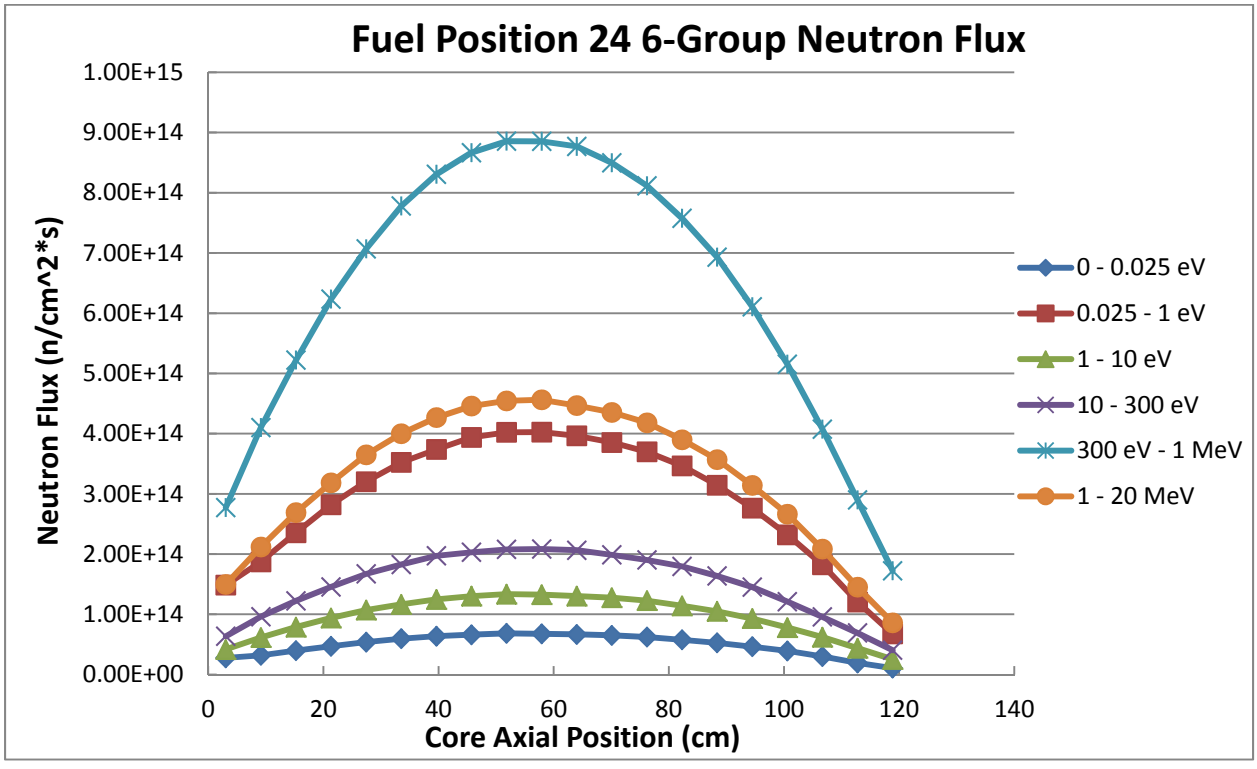

Figure 20. Neutron flux distribution in the approximation of 6 energy groups for the fuel element in position 24, SE ATR lobe.

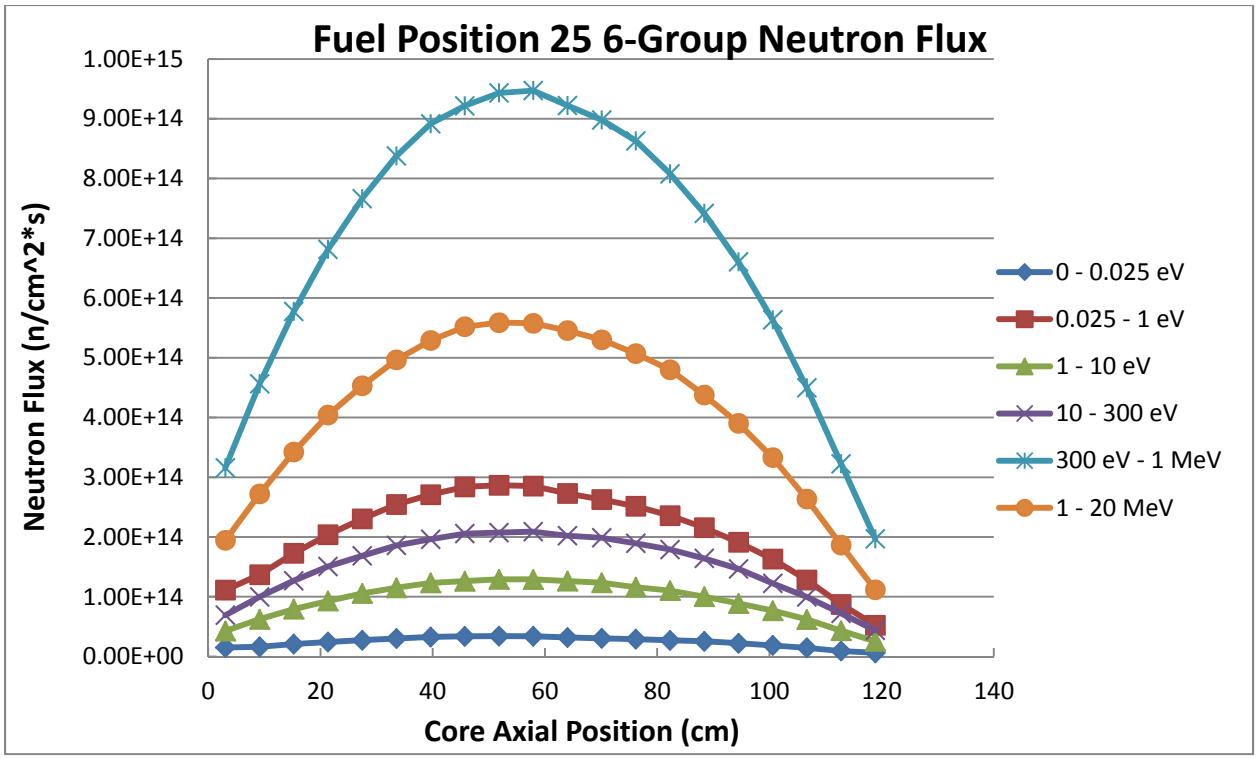

Figure 21. Neutron flux distribution in the approximation of 6 energy groups for the fuel element in position 25, SE ATR lobe.

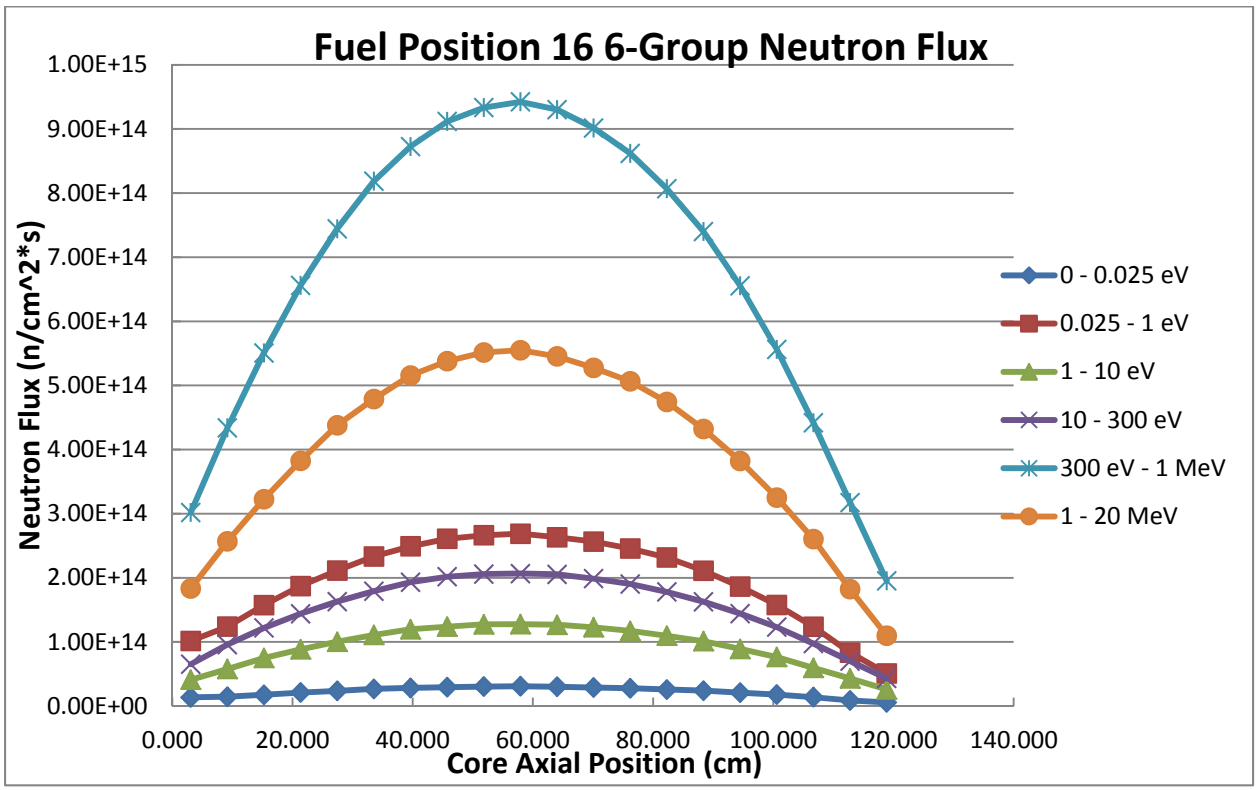

Figure 22. Neutron flux distribution in the approximation of 6 energy groups for the fuel element in position 16, SW ATR lobe.

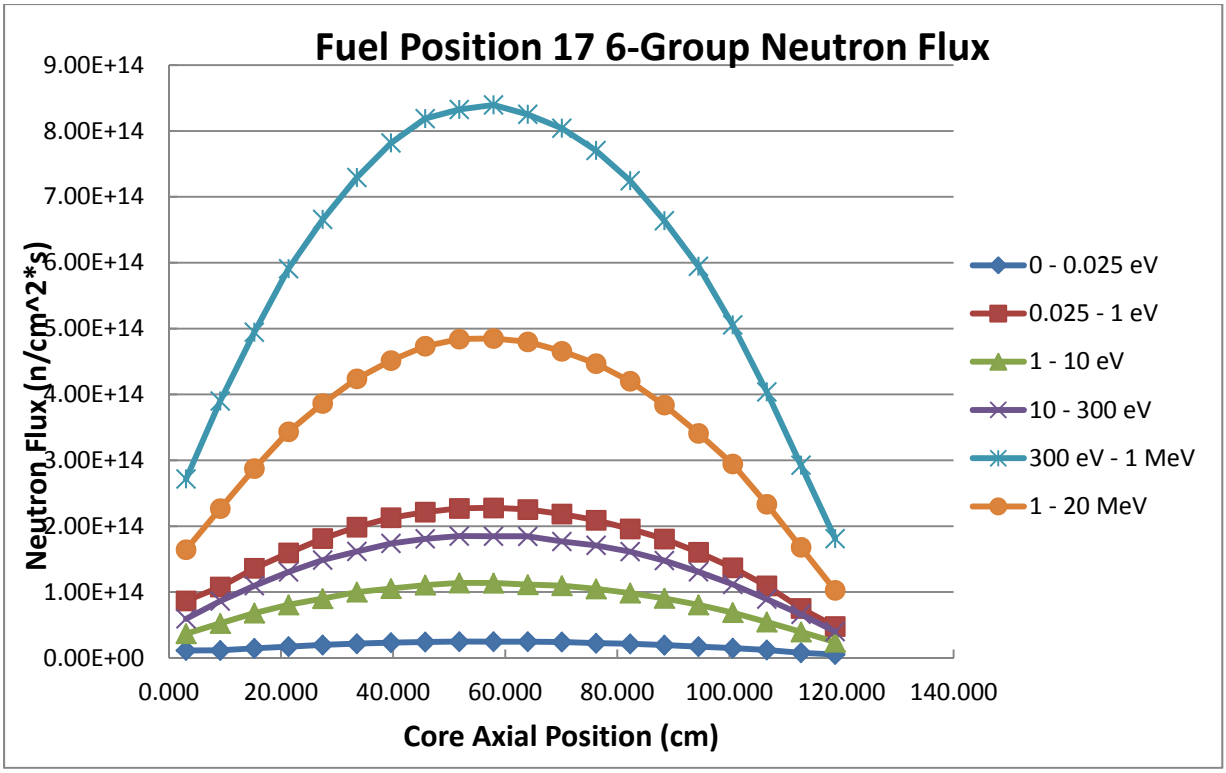

Figure 23. Neutron flux distribution in the approximation of 6 energy groups for the fuel element in position 17, SW ATR lobe.

The maximal values of the neutron flux were realized in the central part(s) of the corresponding elements, which may contribute to the observed corrosion/erosion described in Section 1 of this Report.

Based upon the obtained results, one can hypothesize that the influence of the neutron flux is not limited just to heat generation in the cooling channel 20. Additionally, the neutron fluence can affect preferentially the grain boundary segregated chemical elements with high (comparing to the aluminum matrix) values of neutron absorption cross-sections. While this factor might not be important for the fuel elements inside the reactor, it can play a certain role for the "dummy" plates (i.e., without fuel) and contribute to the phenomenon if intergranular stress corrosion cracking (IGSCC). To verify this hypothesis, more detailed metallurgical modeling of grain boundary segregation along with the assessment of the radiation-induced damage will be warranted. Such a probabilistic damage assessment could be conducted using the sequence of the following software codes: HELIOS (neutronics) → MCNP (3D-neutron flux reconstruction) → ORIGEN (software for isotope generation and depletion analysis)

During the initial analysis of the process a decision was made to introduce the necessary corrections for the heat flux distribution in the axial direction. These corrections were made using the "after cycle" data for cycle 153B using the "HELIOS" software.[11] At this time, HELIOS is in the implementation stage at ATR and will be used for the Core Physics Analysis of all fuel campaigns at ATR. What distinguishes HELIOS from the previously used software is that the ATR model was constructed in 2D-space. Consequently, it is necessary to transform the model into 3D using the MCNP code. For that goal, using HELIOS the 49 energy group neutron distribution was obtained that corresponded to the 153B PALM cycle. Then, the total number of energy groups was reduced to 6 and, using these results, calculations were conducted for the values of heat flux along the whole channel 20. In turn, these results were used in thermo-hydraulic super-computer calculations reported in the next section.

4. THERMO-HYDRAULICS SUPERCOMPUTER MODELING

The boundaries of the model were the aluminum EE plate of a YA-M fuel element and a beryllium reflector block with 13 horizontal saw cuts which represented regions of zero flow. The heat generated in fuel plates 1 through 18 was modeled to be passing through the aluminum EE plate. The coolant channel 20 width was set at 0.058 in. (58 mils). The horizontal saw cuts had a significant effect upon the temperature of the coolant. The flow, which was expected to linear with gradual heating of the coolant as it passed through the channel, was turbulent. The temperature rise, which was expected to be a smooth "S" curve, was represented by a series of seemingly random, temperature rise "humps," which occurred at each horizontal saw cut in the beryllium reflector block. Each of the 13 saw cuts had a chamfered edge which resulted in the coolant flow being re-directed as a jet across the coolant channel into the surface of the EE plate, which explained the seemingly random temperature rise and the observed pitting degradation on the YA-M fuel elements.

In order to confirm these results two additional calculations were performed. The same computer model was repeated with the coolant channel 20 width increased by 50 percent. The temperature rise along the length of the coolant channel was a smooth "S" curve. The narrow dimension of coolant channel 20 on a YA-M fuel element was a significant contributor to the observed flow erosion on the EE plates.

In order to determine if the chamfer on the edge of the horizontal saw cuts was significant, the original model was re-run with a simulated larger chamfer on the edge of the saw cut, and the jetting affect was reduced significantly. A proposal was suggested to modify the chamfer on the edge of beryllium reflector block prior to the next planned CIC in 2020. All eight beryllium reflector blocks have already been fabricated and shipped to the ATR for installation in the core in 2020. The risk of repackaging and returning these beryllium blocks to the fabricator is not worth the benefit to be gained.

The details of the corresponding technical evaluation are presented below.

- Fluid flow is a primary accelerator of erosion within a reactor system. At the Advanced Test Reactor, primary coolant travels through the thin coolant channels between fuel plates at a nominal rate of 47 ft/s during three primary coolant pump operation. Three PCPs, rather than two PCPs, are required every time when the ATR is run in the PALM cycle mode to ensure that the required cooling is provided inside the reactor. The primary goal of this section is to illustrate the thermo-hydraulic modeling conducted to explain how the turbulent coolant flow interacts with the YA plate 19 face, as well as how the coolant flow is affected by the non-uniformly distributed stress-relief cuts in the beryllium reflector blocks, illustrated in Figure 6.
- More specifically, degradation of the Aluminum 6061 on the face of the YA plate in channel 20 was the goal of this part of the present study. It is clear that the system of horizontal cuts in Be (aimed to arrest propagation of large vertical cracks) introduced additional perturbation into the coolant flow in channel 20 and, potentially, could exert influence upon different degradation processes that were observed on the Plate 19 outer surface. This thermos-hydraulic modeling was conducted because no existing analysis of the stress relief cuts in the Be block could be found.
- Power, heat flux, temperature, and coolant flow in the SW lobe during Cycle 153B-1 were used as inputs for the following simulations.

4.1 Modeling Assumptions

- All of the models assume three-pump operation, unless indicated.
- Inlet is set to "velocity inlet" boundary condition with a velocity of 47 ft/s.
- The models assume a heating profile from plate 19 that directly correlates to the thermal neutron flux (see following section for derivation). Only neutrons between 0 – 10 eV contribute to this flux.

- Outlet is set to pressure boundary condition with zero pressure gage.
- Due to the very high turbulence of the system, a wall slip condition is used for the wall boundaries.
- Inlet coolant temperature is 125°F.

4.2 Supporting Calculations

- Plate 19 is assumed to be a cosine-shaped heat source in the model. The heat source directly correlates to the neutron flux in plate 19 (despite no fuel in that plate) and serves as a very rough approximation. This heat source was calculated via the following reaction rate equation:
- $Q(x) = \varphi(x) * \sigma_{thermal} * N_a * C$
- The thermal neutron cross section was taken from Appendix A of Duderstadt and Hamilton[13]: $\sigma_{thermal} = 577\ b\ (5.77 * 10^{-22}\ cm^2)$
- The atomic number density of U-235 in ATR Al-U composite fuel is:

  1.135E22 #/cm^3 (for 72 wt% U – upper bound. Source: EGG-PRP-8783 [14])
- The neutron flux provided by Reactor Engineering was fitted with a second-order polynomial to allow the profile to be programmed into the modeling software. 0 - 10 eV neutrons were used.
- $P(x) = \varphi(x) * \sigma_{thermal} * N_a = \ -1\text{E}15(\text{X} - 0.1)^2 \ + \ 1\text{E}15(\text{X} - 0.1) \ + \ 1\text{E}14\ \frac{n}{cm^2 s}$
- $C = energy\ conversion * plate\ volume = \frac{200 MeV}{fission} * \frac{3.2 * 10^{-11} J}{MeV} * 3.638\ cm^3 = 7.625 * 10^{-11}\ \frac{J\ cm^3}{fission}$
- $\therefore Q(x) = P(x) * C = \frac{n}{cm^2 s} * cm^2 * \frac{1}{cm^3} * \frac{J\ cm^3}{fission} = W$
- $Q(x) = [-1\text{E}15(\text{X} - 0.1)^2 + \ 1\text{E}15(\text{X} - 0.1) \ + \ 1\text{E}14]\ \frac{n}{cm^3 s} \ * \ 7.625\text{E} - 10\ \frac{J\ cm^3}{fission}$
- $Q(x) = \left[-1\text{E}15(\text{X} - 0.1)^2 \ + \ 1\text{E}15(\text{X} - 0.1) \ + \ 1\text{E}14\right] \ * \ 7.62E - 10\ W$

4.3 Coolant Velocity and Temperature Distribution in the Cooling Channel with Non-Uniformly Distributed Cuts in Be Neutron or Block

Initial results of the thermo-hydraulic model indicated that at each of the stress-relief cuts a large velocity discontinuity occurs, resulting in a sharp increase and subsequent drop-off in coolant velocity. Additionally, the temperature profile at the plate face was not the expected linear increase; two distinct maxima are present near the top and bottom of the coolant channel. Specifically, these maxima are 1) just before the third cut, and 2) just after the last, or 13th, cut. The results of this standard case are shown in Figure 24.

A second case was run using the same parameters but reducing the inlet velocity to two-pump operation (43 ft/s) to investigate the velocity and temperature profiles. Figure 25 shows the results of the two-pump operation with nearly identical results. The main difference between two and three pump operation is the coolant velocity magnitude, as expected. The slight reduction in flow resulted in slightly higher temperatures with all other input parameters held constant.

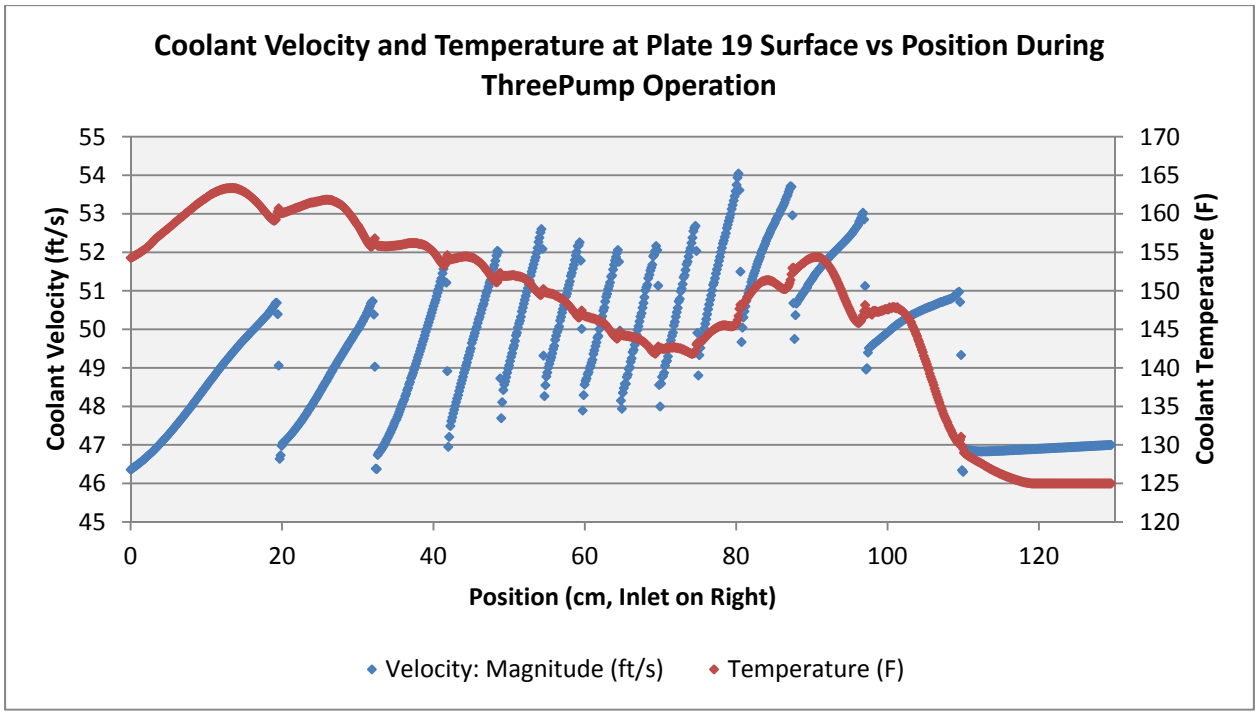

Figure 24. Cycle 153B; Coolant velocity and temperature vs position for three primary coolant pumps in Coolant Channel 20.

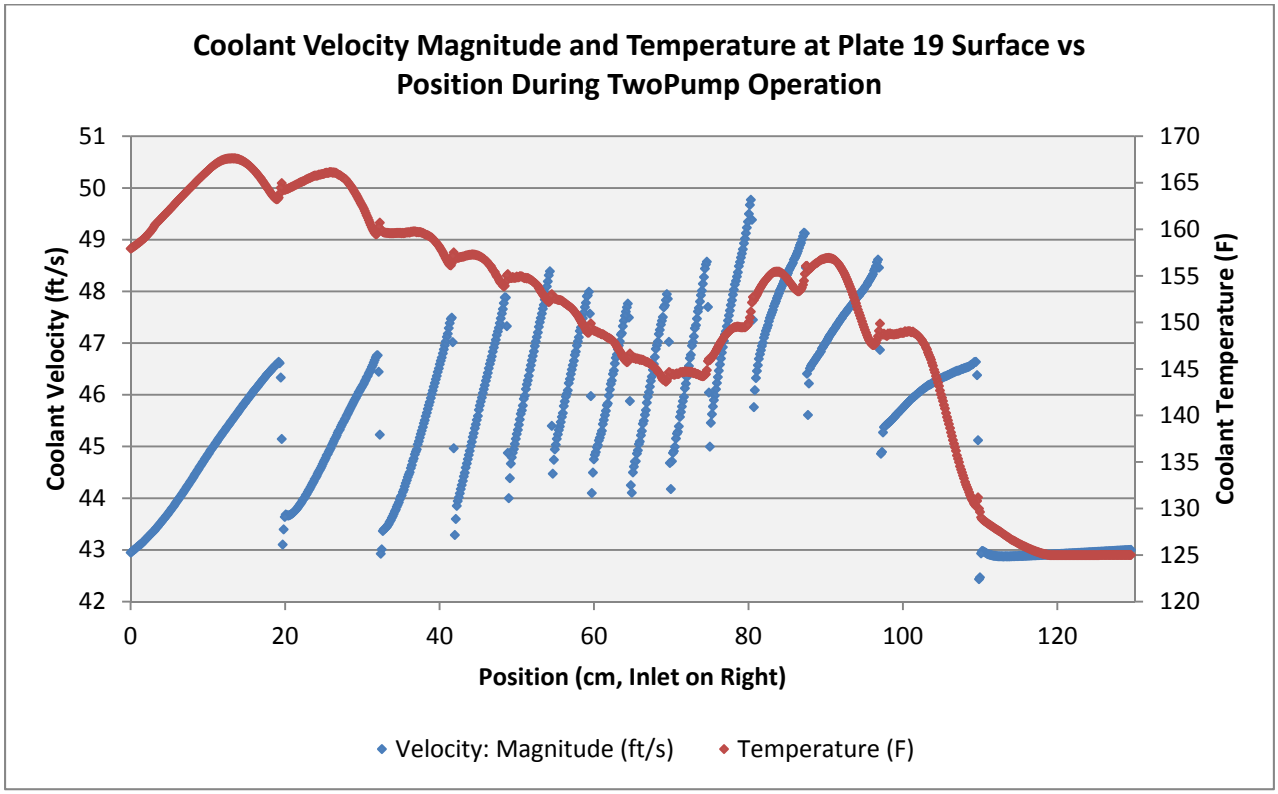

Figure 25. Cycle 153B; Coolant velocity and temperature vs position for two primary coolant pumps in Coolant Channel 20.

A plausible explanation of this dual-maximum effect can be explained by the development of strong cooling fluid flow perturbations immediately after a given horizontal cut, which plays the role of a "turbulence inducer." This can be clearly seen from Figures 26 and 27 illustrating that the flow stabilizes at a certain distance from the perturbation originating cut.

The first horizontal cut creates a turbulent flow condition that exasperates the flow erosion four inches from the top of the plate. The turbulent flow conditions exist between all subsequent saw cuts, which can be used to explain observed flow erosion corrosion material. Only after the last, 13th saw cut does the flow stabilize and the flow erosion corrosion stop for the last few inches of plate 19.

These considerations can be quantified using a semi-empirical formula[13,1415,16]:

$$x_o \geq 0.6 \cdot D_o \cdot \mathrm{Re}^{0.25} \tag{1}$$

In this expression D_0 stands for the channel diameter, Re is the Reynolds number and x_0 stands for the distance (from the perturbation site) at which the flow stabilizes hydro-dynamically. This distance turned out to be equal to 1.063 – 1.181 in from the exit surface of the cut. Applying this idea to the analysis of the graph in Figure 28, one can come to the conclusion about validity of this statement. Indeed, this is well confirmed by the appearance of the secondary peaks in the areas in between two adjacent cuts. Note that the distance between cuts, shown in Figure 6, decrease in distance when closer to core mid-plane. The closest cuts (7 and 8) are only two inches apart, whereas the distance between the first and second cut is five inches apart. While the flow stabilizes roughly after an inch per the formula above, the short distance (as low as two inches) between cuts near the mid-plane may still prevent the flow from stabilizing.

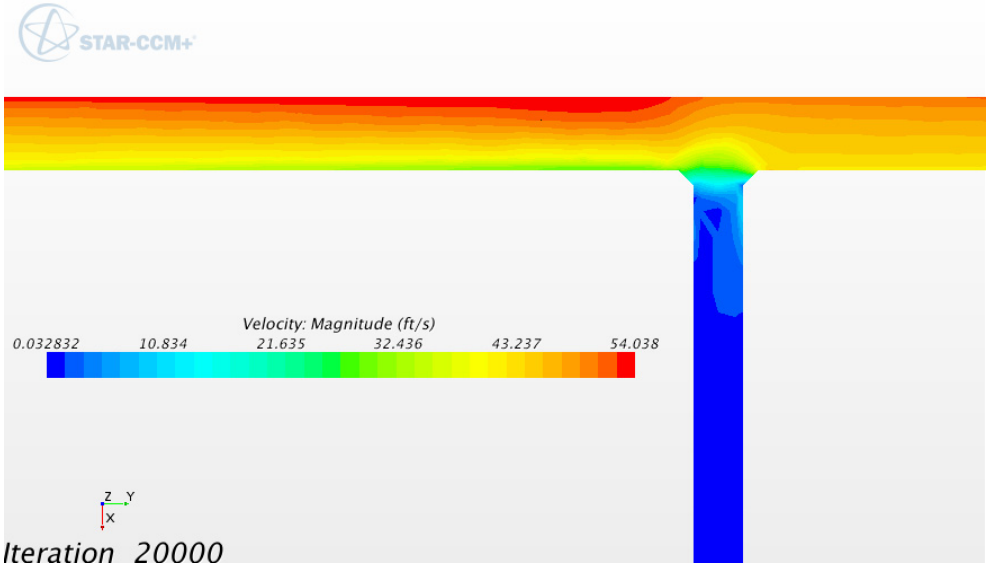

Figure 26. Flow structure: velocity distribution field around the cut in beryllium reflector block.

According to Reference 17, the essence of this flow phenomenon is in the formation of a stable turbulent sublayer, in which heat exchange is much lower than in strongly turbulent "core" at the site of the local perturbation, directly after the cut downstream. This assumption helps explain the specific profile of the temperature distribution in the coolant flow.

To further explore and verify the temperature profile of these standard cases, the coolant channel geometry was modified. Instead of 13 cuts, only three were used (no. 1, no. 7, and no. 13). The results in Figure 28 demonstrate that the distribution profile (shape) depends almost exclusively upon the absence or presence of horizontal cuts and their total number.

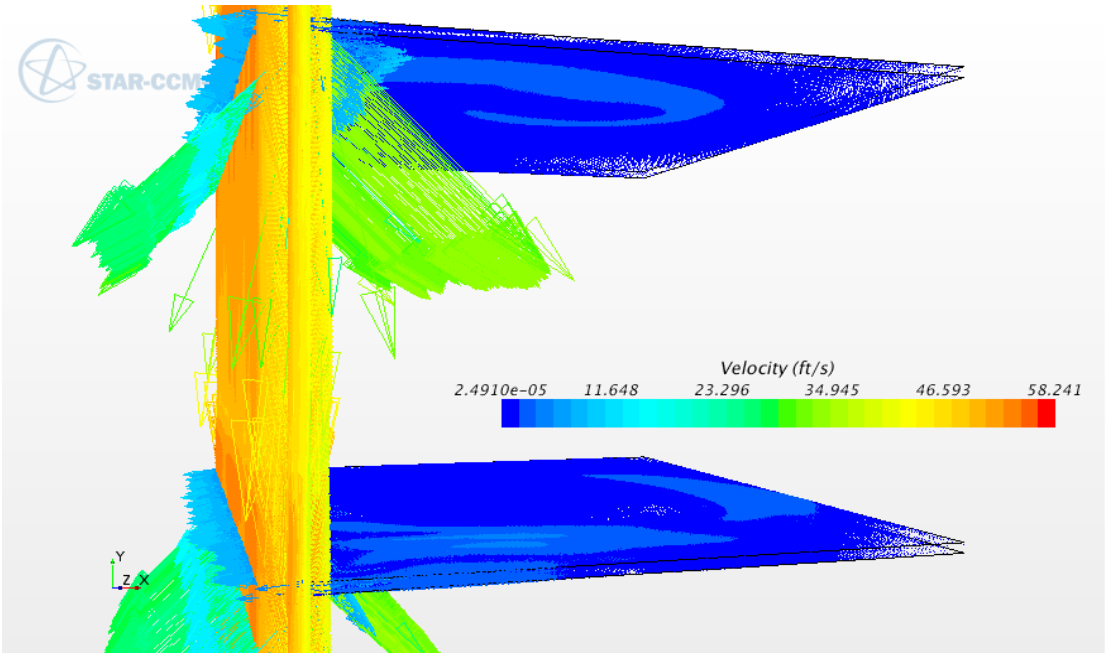

Figure 27. Flow Structure in 3D: the same as the previous figure, but with a vector field distribution for flow velocities in the direct vicinity of the cut. Perturbations from the stress-relief cuts cause the coolant to flow into the plate face at up to 35 ft/s.

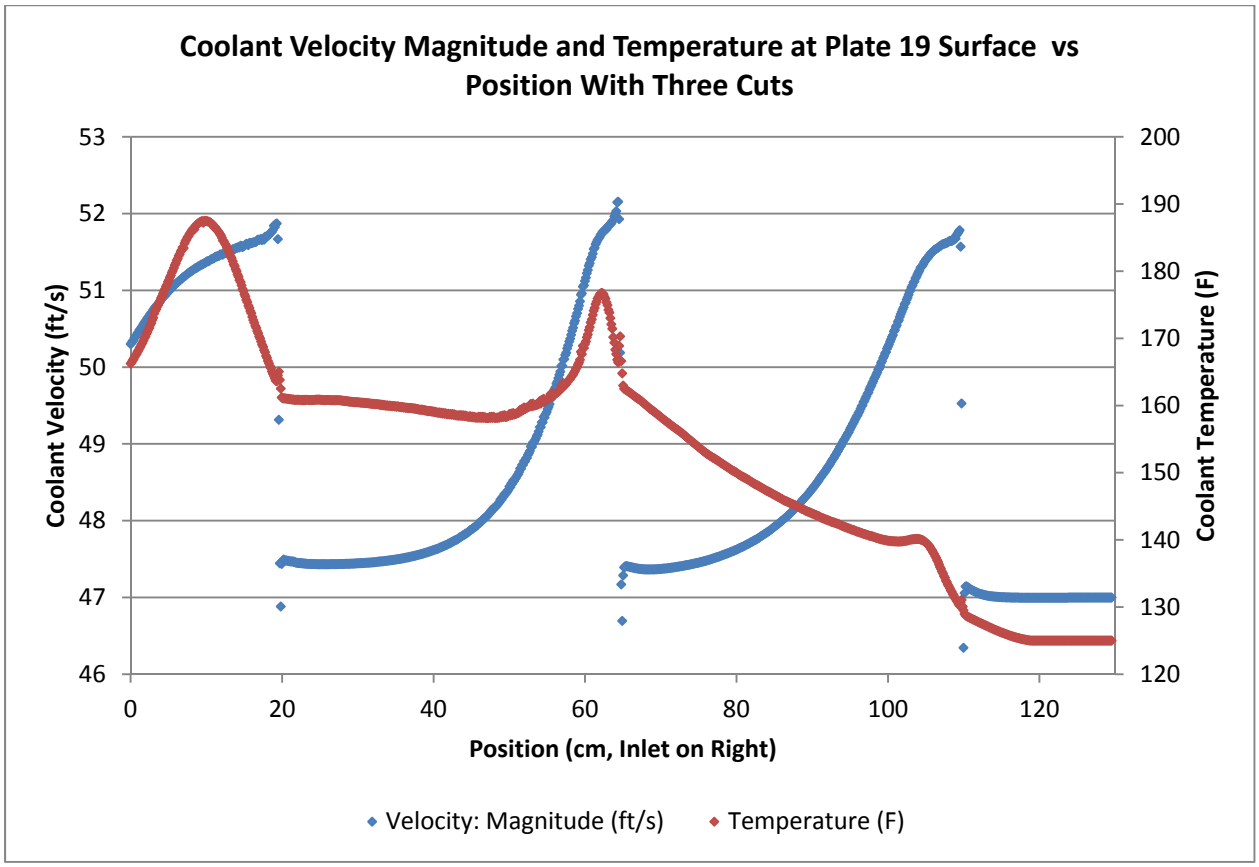

Figure 28. Cycle 153B; coolant velocity and temperature vs position – system with three cuts.

While the phenomena detailed above may cause the coolant temperature profile at the plate surface to appear strange, the temperature profile of the bulk coolant still exhibits the expected "S" curve, as shown in Figure 29.

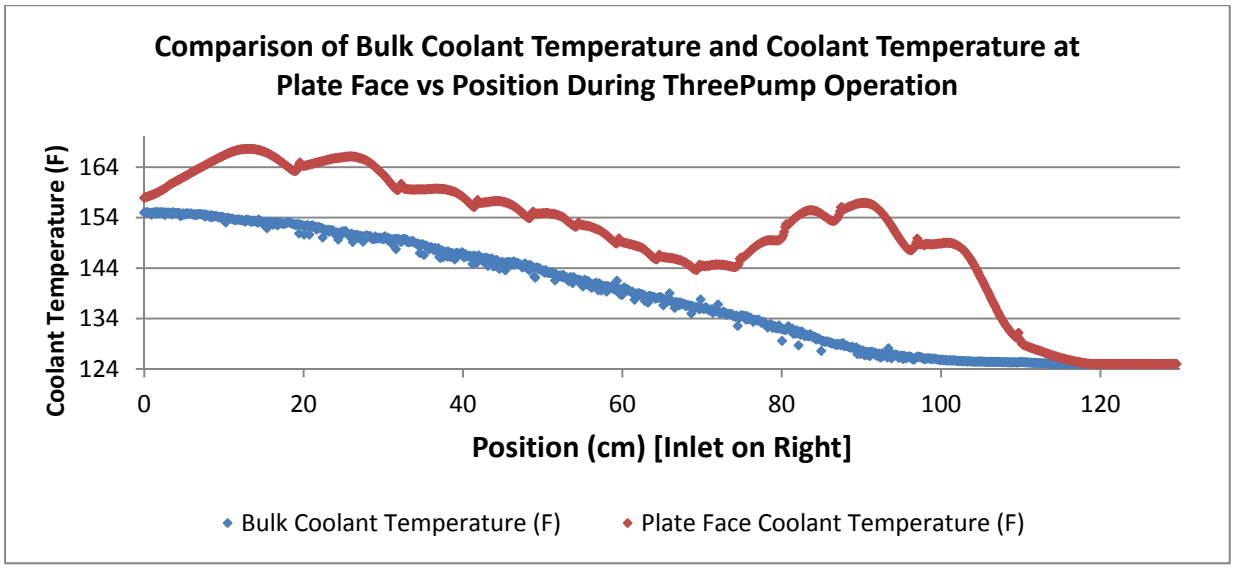

Figure 29. Cycle 153B; coolant temperature at the plate face compared to bulk coolant temperature.

4.4 Deep Chamfer Cuts

As these simulations identified erosion as a possible primary contributor to the YA-Plate 19 pitting degradation issue, the channel geometry was further modified to attempt to find a solution to the post-cut flow perturbations. A proposed solution was to exaggerate the chamfer on the bottom of the cut to observe how this change affected the solution, even though this change would likely not be beneficial as the reflector block ligaments are only 1/8 in. thick. Figure 30 shows the model geometry at a single cut site and the velocity magnitude as a result of the modification. The new bottom, "deep" chamfer is 1/8 in. deep, compared to 1/64 in. in the standard case.

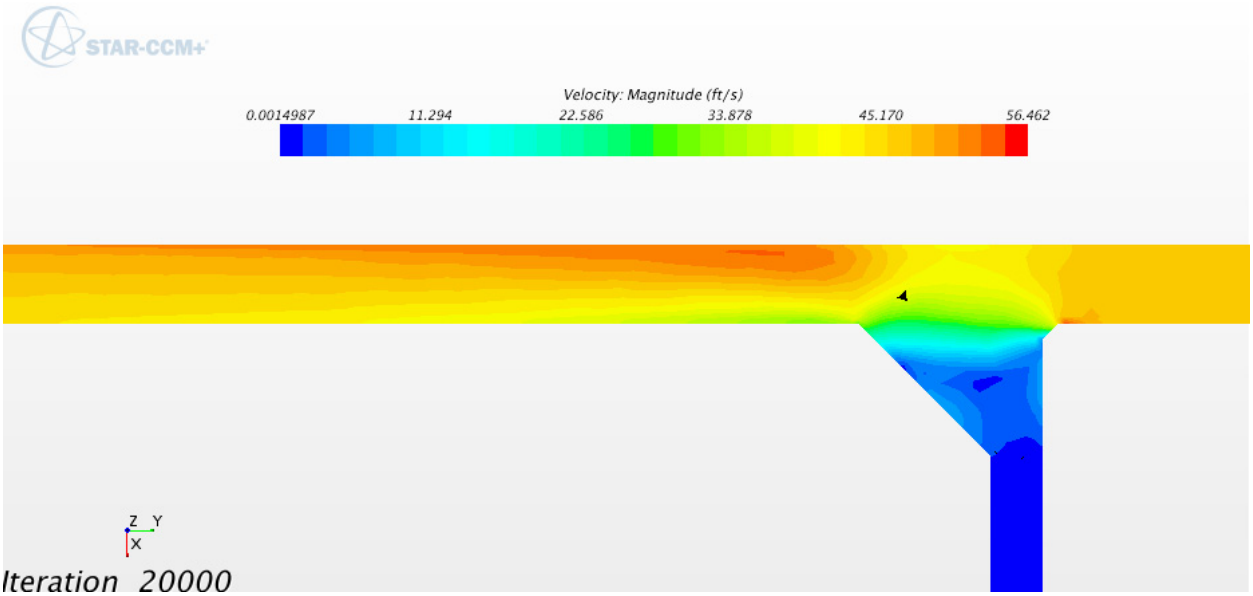

Figure 30. Flow structure: velocity distribution field around the cut in beryllium reflector block with a modified (1/8 in.) bottom chamfer.

The chamfer modification had a modest impact on the coolant velocity vectors. There are still velocity vectors toward the plate, but these are reduced in number and much more spread out axially.

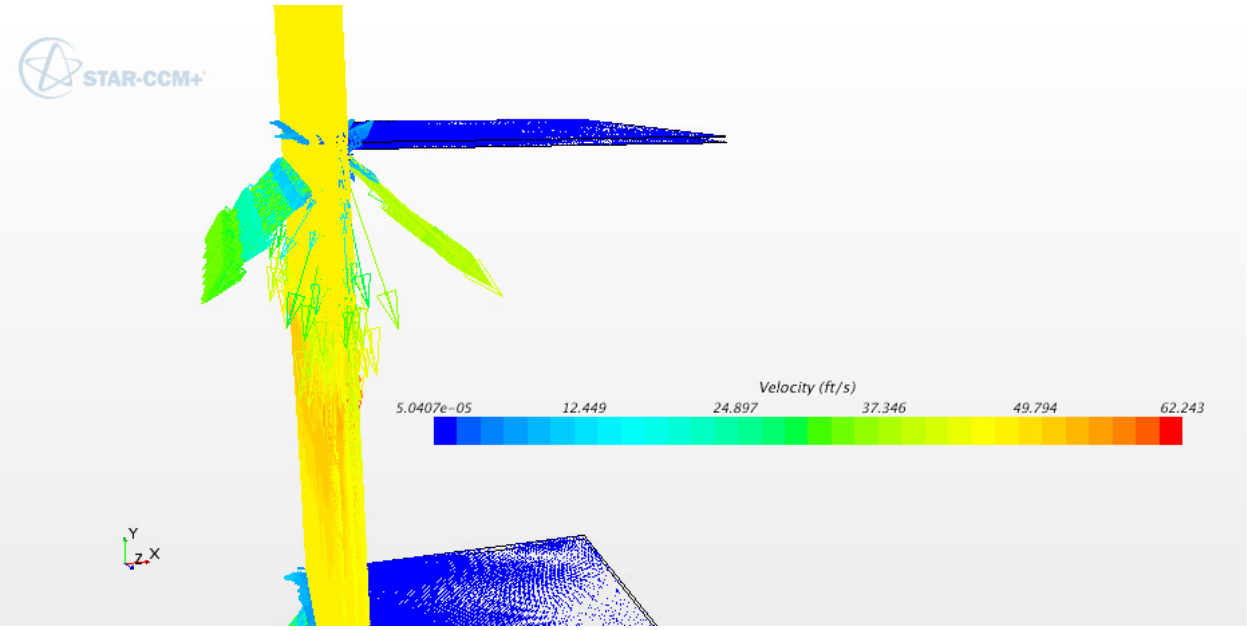

Figure 31. Flow structure in 3D: the same as the previous figure, but with a vector field distribution for flow velocities in the direct vicinity of the cut.

Figure 32 shows the velocity and temperature profiles versus axial position with the modified chamfer. While the magnitude at the discontinuity is not markedly different than the standard case, it is important to note that the temperature is significantly more linear and is lacking the dual-maxima of previous cases.

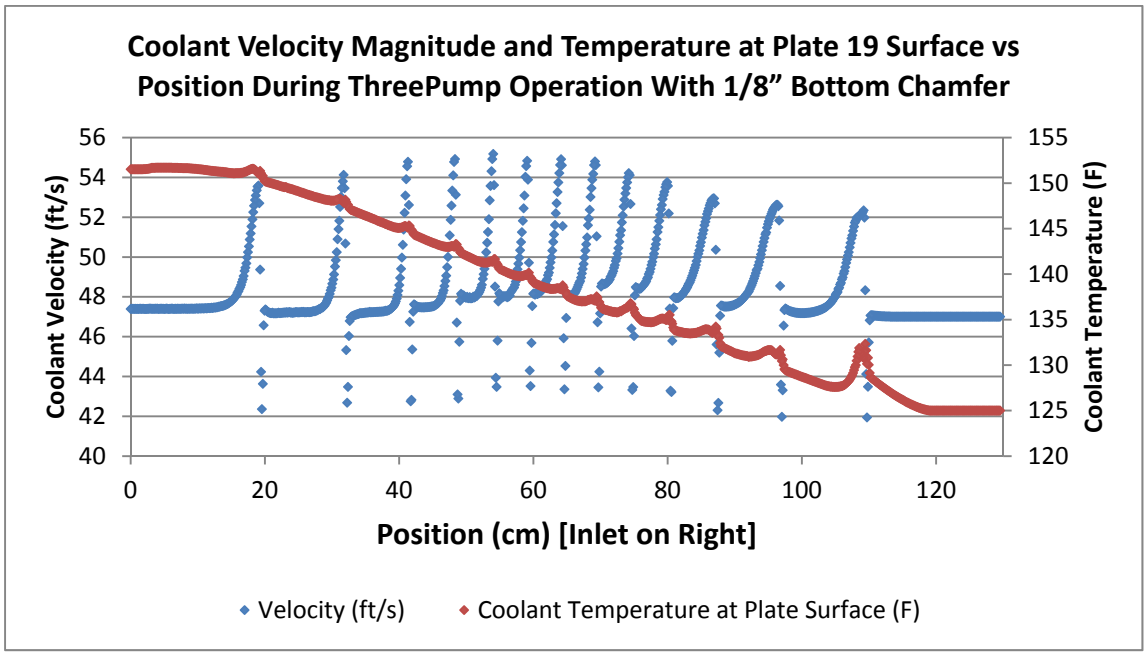

Figure 32. Velocity magnitude/temperature at the Plate 19 surface. While the discontinuities still exist with the modified chamfer, it is important to note that the magnitude does not say anything about the direction of the flow.

The coolant channels have never been analyzed thermo-hydraulically, and the results of these simulations match some empirical observations, such as enhanced erosion bands at the Be stress-relief locations. Thus, one can conclude with a high degree of probability that one of the main contributions to the observed erosion phenomena is turbulent flow created by the horizontal stress-relief saw cuts in the Be reflector.

5. CONCLUSIONS

In this technical report the results of interdisciplinary multi-physics simulations and experimental work are documented. The role of the several important factors potentially affecting erosion behavior of the aluminum 6061 "dummy" plate was evaluated, paying special attention to such methods and techniques as computational thermodynamics and kinetics of phase transformations (Thermo-Calc and JMatPro); neutronics modeling using MCNP and HELIOS; thermal-hydraulics modeling using supercomputer modeling with STAR-CCM+.

As a result of conducted studies, a request was submitted to BWXT to revise the fabrication process for the EE dummy plates to include an additional blister anneal at 900°F (482°C) for 2 hours. The first YA-M fuel elements to be fabricated using the revised process are scheduled to be fabricated in 2016, and are expected to be loaded in the ATR core in 2017, so several years will pass before the effects of the additional blister anneal of the EE plate can be evaluated.

The higher reactor power levels associated with high power PALM cycles require three primary coolant pump operation, as opposed to two pump operation for lower power cycles. The higher power of a PALM cycle results in higher coolant temperatures, but that is somewhat offset by higher primary flows through the core. The primary coolant inlet temperature is 125°F, and at 250 MW the coolant outlet temperature is 170°F, with less temperature rise across the core at power levels less than 250 MW. The minor increase in fuel plate and primary coolant temperatures due to the operating conditions during a high power PALM cycle may have contributed to the observed pitting degradation. All neutronics simulations were conducted using such codes as MCNP and HELIOS, with the goal of obtaining the necessary input data for subsequent thermal-hydraulics simulations.

As a result, a thermal-hydraulic model of coolant channel 20 on a YA-M fuel element was generated. The boundaries of the model were the aluminum EE plate of a YA-M fuel element and a beryllium reflector block with 13 horizontal saw cuts which represented regions of zero flow. The heat generated in fuel plates 1 through 18 was modeled to be passing through the aluminum EE plate. The coolant channel 20 width was set at 0.058 in. (58 mils). The horizontal saw cuts had a significant effect on the temperature of the coolant.

The flow, which was expected to vary linearly with gradual heating of the coolant as it passed through the channel, was extremely turbulent. The temperature rise, which was expected to be a smooth "S" curve, was represented by a series temperature rise "humps," which occurred at each horizontal saw cut in the beryllium reflector block. Each of the 13 saw cuts had a chamfered edge which resulted in the coolant flow being re-directed as a jet across the coolant channel into the surface of the EE plate, which explained the temperature rise and the observed pitting degradation on the YA-M fuel elements.

In order to confirm these results two additional calculations were performed. The same computer model was repeated with the coolant channel 20 width increased by 50 percent. The temperature rise along the length of the coolant channel was a smooth "S" curve. The narrow dimension of coolant channel 20 on a YA-M fuel element was a significant contributor to the observed flow erosion on the EE plates.

In order to determine if the chamfer on the edge of the horizontal saw cuts was significant, the original model was re-run with a simulated larger chamfer on the edge of the saw cut, and the jetting affect was reduced significantly. A proposal was suggested to modify the chamfer on the edge of beryllium reflector block prior to the next planned CIC in 2020. All eight beryllium reflector blocks have already been fabricated and shipped to the ATR for installation in the core in 2020. The risk of repackaging and returning these beryllium blocks to the fabricator is not worth the benefit to be gained.

6. REFERENCES

1. 1. S. A. Hill letter to C. D. Cooper, Advanced Test Reactor (ATR) Cycle 153B-1 Post-Use Fuel Element Visual Inspection, SAH-07-13, May 13, 2013
2. S. L. Denison letter to J. O. Brower, Advanced Test Reactor Pitted YA Fuel Element Oxide and Channel Measurements, SLD-01-14, January 7, 2014
3. J. O. Brower letter to R. A. Jordan, Advanced Test Reactor Fuel Element Oxide and Channel Measurements for Pitted YA Fuel Elements, JOB-06-14, April 30, 2014
4. S. A. Hill letter to J. O. Brower, Advanced Test Reactor Pitted YA Fuel Element Oxide and Channel Measurements from Cycles 156A-1 and 157A-1, SAH-29-14, November 17, 2014
5. J. O. Brower letter to R. A. Jordan, Advanced Test Reactor Fuel Element Oxide and Channel Measurement Results for Cycles 156A-1 and 157A-1, JOB-15-14, December 15, 2014.
6. IN-F-9A-ATR, Specification for ATR Special Non-Fueled Plate 19 7F Fuel Elements, May 28, 1992.
7. FCF ATR 7.7.1/ATRF-001, Non-Fueled Plate 19 ATR Fuel Elements, October 2, 1975.
8. FCF-7.2.1-3/ECF-3171, Modified Non-Fueled (YA) Plate 19 ATR Fuel Elements, August 3, 1995.
9. TEV-2090, Technical Evaluation ATR YA-M Type Fuel Element Aluminum Plate 19 Damage Acceptance Criteria, February 12, 2014.
10. T.A. Tomberlin, Advanced Test Reactor (ATR) Reflector Safety Analysis, PG-T-89-018, Rev. 0, July 1, 1989.
11. Advanced Test Reactor (ATR) Cycle 153B-1 Fuel Element Loading Revision 1, INL Interoffice Memorandum, March 20, 2013
12. E. Shaber and G. Hofman, Corrosion minimization for Research Reactor Fuel, INL/EXT-05-00256 (June 05, 2016)
13. D.A. Jones, Principles and Prevention of Corrosion, McMillan, New York (1992).
14. J. Lafuente, O. Navara, J.E. Rosa da Silva, J.K. Dalidet, R. Sindelar, Damage Degree Classification for MTR Type Spent Fuel in Wet Interim Storage, 10th International Topical Meeting on Research Reactor Fuel Management, Sofia, Bulgaria, April 30 –May 4, 2006.
15. N. Wolstenhumme (INL), private communication (July 2014)
13. D.A. Jones, Principles and Prevention of Corrosion, McMillan, New York (1992).
14. J. Lafuente, O. Navara, J.E. Rosa da Silva, J.K. Dalidet, R. Sindelar, Damage Degree Classification for MTR Type Spent Fuel in Wet Interim Storage, 10th International Topical Meeting on Research Reactor Fuel Management, Sofia, Bulgaria, April 30 –May 4, 2006.
15. N. Wolstenhumme (INL), private communication (July 2014)
16. K. Wefers, and C. Misra, Oxides and Hydroxides of Aluminum, Alcoa Laboratories Technical Paper No. 19, Revised, 1987.
17. S.N. Rashkeev, K. Sohlberg, M.V. Glazoff, J.W. Novak, S.J. Pennycook, and S.T. Pantelides, Transition Metal Atoms on Different Alumina Phases: The Role of Subsurface Sites on Catalytic Activity. *Physical Review B (Condensed Matter)*, vol.67, 115414 (2003).
18. G. S. Frankel, J. R. ScuIIy, and C. V. Jahnes, Repassivation of Pits in Aluminum Thin Films, *J. Electrochem. Soc.*, Vol. 143, No. 6, June 1996.

19. L. Organ, J.R. Scully, A.S. Mikhailov, J. L. Hudson, A spatio-temporal model of interactions among metastable pits and the transition to pitting corrosion, *Electrochimica Acta,* vol.51 pp. 225–241 (2005).

20. Miglin, B. P., Production of Boehmite Film on Aluminum, Babcock & Wilcox Alliance Research Center, September 1994.

21. Corrosion of Research Reactor Aluminum Clad Spent Fuel in Water, IAEA Technical Report Series, Report no. 418, Chapter 3; Guidelines for Corrosion Protection of Research Reactor Aluminum Clad Spent Nuclear Fuel in Interim Wet Storage, pg. 56-60. Vienna (2003).

22. Joseph M. Beeston, Lowell G. Miller, Keith R. Brown, David M. McGinty, ELAF Fuel Plate Examination, EG&G Idaho, October 1984.

23. M.L. Griebenow, G.H. Hansen, A.P. Larrick, TRA Oxide Film Control and Surveillance (a Reference Document), INEL, RE&C Report RE-A-77-059, October 1977.

24. J.C. Griess, H.C. Savage, J.L. English, Effect of Heat Flux on the Corrosion of Aluminum by Water, Part IV. Tests Relative to the Advanced Test Reactor and Correlation with Previous Results, ORNL Contract No. W-7405-eng-26, February 1964.

25. G.L. Hofman to J.L. Snelgrove, Corrosion of Iowa State University UTR-10 Fuel Plates, Preliminary Report, Argonne National Laboratory, June 10, 1993.

26. E.L. Shaber, Iowa State Research Reactor Fuel Cladding Surface Quality Evaluation, INEEL, EDF-TRA-ATR-1437, 3/19/1999.

27. E.L. Shaber, Micro-Pitting of 6061-O Aluminum Fuel Plates During Hydroxide Coating, INEEL, EDF-730, Rev 0, 2/18/1998.

28. S.P. Henslee, ATR Fuel Element Pitting, INEL, Report PR-T-80-030, April 1980.

29. J.M. Beeston, ETR Fuel Element Pitting, INEL, Report RE-M-78-012, April 1978.

30. Fuels and Materials Development Program Quarterly Progress Report for Period Ending December 31, 1968, Compiled by P. Patriarca, Ed. by D.J. Rucker, ORNL, Contract No. W-7405-eng-26, May 1969.

31. (Recrystallization Behavior of Rolled Ingots of 6061 and 6069 Aluminum Alloys, X. Li, M.E. Kassner, and S.C. Bergsma, *JMEPEG* (2000) vol. 9 pp. 416-423).

32. P.J. Withers, 3D- materials characterization over a range of time and length scales, *Advanced Materials and Processes*, pp. 28-32 (June 2012).

33. http://www.fei.com/products/dualbeam/helios-pfib-for-electronics/ (2015).

34. Teal Sheets - International Alloy Designations and Chemical Composition Limits for Wrought Aluminum and Wrought Aluminum Alloys, published by the Aluminum Association (February 2009).

35. D.J. Chakrabarti, D.E. Laughlin, Phase relations and precipitation in Al–Mg–Si alloys with Cu additions, *Progress in Materials Science*, vol.49, pp.389–410 (2004).

36. K.I. Matsuda, M. Susumu, Hiroaki; T. Sato, K. Terayama, Y. Uetani, Comparison of Precipitates between Excess Si Type and Balanced-Type Al-Mg-Si Alloys during Continuous Heating, *Metallurgical and Materials Transactions A*, vol. 36, N 8, pp. 2007- 2012 (2005).

37. I.J. Polmear, Light Metals: Metallurgy of Light Metals, Halsted Press, 1995.

38. http://www.sentesoftware.co.uk/.

39. V.S. Zolotorevsky, N.A. Belov, M.V. Glazoff, Casting Aluminum Alloys, Elsevier, Amsterdam (2007).

40. E. Linardia, R. Haddada and L. Lanzania, Stability analysis of the Mg_2Si phase in AA 6061 aluminum alloy, *Procedia Materials Science* 1 (2012) 550 – 557.

41. James J. Duderstadt and Louis J. Hamilton, *Nuclear Reactor Analysis*, John Wiley & Sons, Inc., New York (1976).

42. Comprehensive Nuclear Materials, By Rudy J.M. Konings (Editor-in-Chief), Section Editors Todd R. Allen, Roger E. Stoller, Shinsuke Yamanaka, Section EGG-PRP-8783, Elsevier, Rotterdam (2012).

43. R.L. Tapping, Corrosion Issues in Pressurized Heavy Water Reactor (PHWR/CANDU) Systems. In: Nuclear Corrosion Science and Engineering, ed. D. Feron, Woodhead Publ. Ltd (2012), p. 634.

44. S.S. Kutateladze, Heat Transfer and Hydrodynamic Resistance, Reference text, Energo-atomizdat, Moscow (1990), in Russian

45. G.S. Was and P.L. Andresen, Irradiation Assisted Corrosion and Stress Corrosion Cracking (IAC/IASCC). In: Nuclear Reactor Systems and Components. In: Nuclear Corrosion Science and Engineering, ed. D. Feron, Woodhead Publ. Ltd (2012), p. 131.